On the determination of the quasi-static evolution of brittle plane cracks via stationarity principle

Gabriele Cricrì °

(°) University of Naples Federico II, Dipartimento di Ingegneria Industriale, P. Vincenzo Tecchio 80, Naples 80125, Italy

Keywords: energy release rate, domain integrals, crack propagation, crack front shape.

Abstract

The crack front evolution in brittle solids is commonly modelled by defining some crack increment criterion, which can be derived from considerations on the stress singularity, from the definition of a dissipative potential, from the introduction of phenomenological concepts such as the crack mobility, and so on. In this work, the problem is faced with no allowance of any crack increment criterion, but using only the elastic properties, the fracture energy, and a stationarity principle. We will show that these ingredients are enough for determining the equilibrium and the quasi-static evolution of generally shaped three-dimensional brittle plane cracks. In doing this, we pointed out some new insight on the crack front motion, a set of new, generalised, domain integrals for measuring the pointwise crack 'tension', and a rigorous calculation of the intersection angle between the crack front and the free surface.

1 - Introduction

The thermodynamic framework, as introduced more than a century ago by Alan A. Griffith (Griffith, 1921), is yet extensively used to model the crack propagation in brittle materials. Since then, the underlying concepts have been clarified, organized, and made useful for the engineering practise through several analytical or numerical approaches. Among the ones relevant for the present article, the variational approach (Francfort et al. 2008), the material or configurational force concept (Gurtin and Podio-Guidugli, 1996; Maugin, 2013), the domain integrals (Steinmann et al. 2001) are worth to be mentioned.

More recently, the regularized variational formulations of the crack surface have becoming popular, like the phase field approach, which can numerically solve, in principle, the general problem of the three-dimensional crack evolution without remeshing needs (see, e.g., Miehe et al., 2010). Nevertheless, models with perfectly bidimensional (sharp) crack in three-dimensional domain are also widely used. In fact, despite the remeshing inconvenience, they still have many worths: only a relatively small number of elements are required, no convergence problems, they do not involve any scale length purely related to the regularization. Further, since the sharp crack model represents the limit behaviour for the regularized models, the first ones are important for benchmarking the second ones.

In this work, the sharp crack front evolution in a three-dimensional domain is faced. To this aim, only the elastic material properties, the fracture energy and a stationarity principle are used. Besides the theoretical aspects, many applications are possible of our results: composites delamination, interface cracks, symmetrical (opening) crack advance, etc. Although the problem may appear well understood, many different methods are used in literature to calculate the crack front evolution, and not all of them converge to the same result. For instance, Ševčík et al., 2012 or Oplt et al., 2019, evaluated the crack front shape by imposing that, at any point of the front, the stress singularity must be constant. In their work, Jiang et al., 2019, defined the crack front at equilibrium as the line along which the strain energy release

rate, calculated via the virtual crack closure technique, is uniform. Further, Vu et al., 2015, utilized to this aim the domain integrals (Destuynder and Djaoua, 1981) plus an independent crack increment criterion. Instead, we will show that, if the stationarity principle is rigorously applied, it is possible to determine the crack front evolution with no allowance of any crack increment criterion.

In section 2, the static equilibrium of a three-dimensional elastic domain with a generic plane crack is formulated as a free energy stationarity problem, which is constrained by the irreversibility. In this way, the equilibrium conditions turn out to be a generalization of the Griffith criterion, applied to each point of the crack front (see, e.g., Moran and Shih, 1987). More precisely, these conditions dictate that the crack increment results to be at equilibrium with the incremented boundary conditions if, at any point of the crack front, the mechanical free energy virtually released for an unitary local crack increment (here named fracture potential) is not higher than the unitary fracture energy.

In section 3, the fracture potential is calculated exploiting the method proposed by De Lorenzi (1982). It turns out to be expressed as the sum of some line and area integrals, to be calculated along the crack front. This result represents a generalization of other well-established ones, obtained using the energy domain integrals (Moran and Shih, 1987), the configurational forces (Gürses and Miehe, 2009) or the Theta method (Destuynder and Djaoua, 1981). Differently from these literature results, the fracture potential can be calculated through integrals not necessarily lying on domains orthogonal to the crack front. For this reason, we can rigorously and accurately calculate the fracture potential also in those points in which the crack front emerges from the external surface of the volume domain, regardless of the intersection angle.

In section 4, the crack propagation problem is faced. The quasi-static propagation can be, in principle, calculated by imposing the static equilibrium at each finite increment of the crack. Hence, it does not need any crack increment criterion based on the physics of the propagation but, instead, an efficient numerical predictor of such increment is sufficient. To this aim, we proposed two different calculation algorithms of the crack front shape. They have been applied to a double cantilever beam (DCB) model subject to opening load and verified to be both efficient. Coherently with the relevant literature, the crack front shape results to be approximately parabolic, being the crack deeper at the inner zones than at the edges. In those points, the intersecting angle of the crack front with the external surfaces turns out to be not constant, but instead increasing with the increasing average crack length.

To the aim verifying the results accuracy, in section 5 the crack front evolution is simulated by modelling the putative crack surface through cohesive elements. We tuned the cohesive law parameters to minimize the process zone length, in order to reproduce as accurately as possible a sharp crack model outcome. The comparison between the resulting crack front shapes calculated through the two different methodologies shows a very sound accordance.

2 – Crack front shape at equilibrium

Let's consider a three-dimensional elastic domain Ω in which a propagating plane crack exists. In fig. 1 the domain is represented with its main descriptive notations. This domain, at a given crack configuration $\boldsymbol{\mathcal{F}_0}$ and given boundary conditions, is associated with a certain mechanical free energy. Adding to the problem description the degree of freedom $\Delta\boldsymbol{\mathcal{F}}$, i.e., the crack increment, the mechanical free energy results enriched, becoming as follows:

$$\phi(\boldsymbol{u},\lambda,\boldsymbol{\mathcal{F}}_0,\Delta\boldsymbol{\mathcal{F}}) = \int_\Omega w(\boldsymbol{u}\backslash\bar{\boldsymbol{u}},\lambda\bar{\boldsymbol{u}},\boldsymbol{\mathcal{F}}_0,\Delta\boldsymbol{\mathcal{F}})dv - \int_{\partial\Omega}\lambda\boldsymbol{Q}\boldsymbol{u}ds \quad (1)$$

where w is the elastic energy density, $\overline{\boldsymbol{u}}$ the constrained subset of the displacement field $\boldsymbol{u}$, $\boldsymbol{u}\backslash\overline{\boldsymbol{u}}$ the unconstrained displacement field, $\lambda\boldsymbol{Q}$ the total external load, and λ the load parameter, possibly applied also to a subset of $\overline{\boldsymbol{u}}$. For simplicity, neither volume forces, nor forces on the crack surfaces are considered in the following.

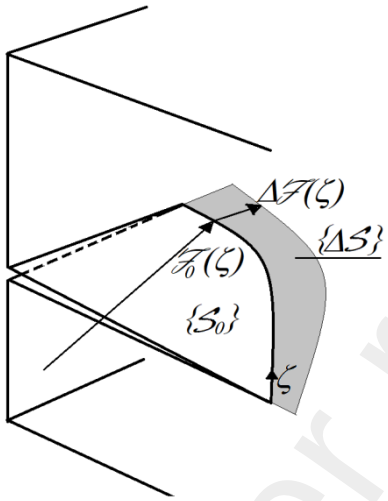

Figure 1 – Crack description. $\{S_0\}$ is the set of points belonging to the initial crack surface; $\{\Delta S\}$ is the set of points belonging to the crack increment surface; $\boldsymbol{\mathcal{F}_0}(\zeta)$ is a vector pointing the initial crack front, whose points are ordered following the normalized curvilinear abscissa ζ[0, 1]; $\Delta\boldsymbol{\mathcal{F}}(\zeta)$ is a vector pointing the incremented crack front, starting from the initial configuration.

The general solution of the elastic problem with a propagating three-dimensional crack does not depend on the crack front shape only, but also on the whole crack surface shape; hence, it depends on the load history. For this reason, one cannot impose the equilibrium via a global minimum principle, but can use instead a local minimum one, consisting of the minimization of the free energy related to the increment of the state variables (see e.g., Francfort et al. 2008). Hence, starting from a given equilibrium condition $(\boldsymbol{u}_0, \lambda_0, \boldsymbol{\mathcal{F}}_0)$, we will seek for the equilibrium depending on the set of the state variables increments $(\Delta\boldsymbol{u}, \Delta\lambda, \Delta\boldsymbol{\mathcal{F}})$. For a general crack shape, these increments must be considered infinitesimal; In case of plane crack (or when the realizable, smooth, crack surface is known in advance) they can be considered finite, unless complicated load histories, not considered here.

Let $\mathcal{E}$ be the fracture energy (or adhesion energy) corresponding to the crack increment $\Delta\boldsymbol{\mathcal{F}}$. It can be interpreted as a configurational free energy and added to the mechanical free energy (1). Hence, the following total free energy functional is obtained:

$$\Pi(\boldsymbol{u_0},\lambda_0,\boldsymbol{\mathcal{F}}_0, \Delta\boldsymbol{u},\Delta\lambda,\Delta\boldsymbol{\mathcal{F}}) = \phi(\boldsymbol{u_0} + \Delta\boldsymbol{u},\lambda_0 + \Delta\lambda,\boldsymbol{\mathcal{F}}_0 + \Delta\boldsymbol{\mathcal{F}}) + \mathcal{E}(\boldsymbol{\mathcal{F}}_0,\Delta\boldsymbol{\mathcal{F}}) \qquad (2)$$

where $(\boldsymbol{u}_0, \lambda_0, \boldsymbol{\mathcal{F}}_0)$ is the initial equilibrium state. The energy Π is naturally interpreted as the free energy of a mechanical system where, compared to the scheme without the crack, the additional energies related to the configurational variables $\boldsymbol{\mathcal{F}}_0,\Delta\boldsymbol{\mathcal{F}}$ and to the fracture energy $\mathcal{E}$ have been made free, that is, made them able to participate to the energies redistribution to attain the incremented equilibrium state. If the propagation was reversible, like for the adhesion problems, the minimum Π would define the (stable) equilibrium state as a function of $\Delta\boldsymbol{u}$, $\Delta\lambda$, $\Delta\boldsymbol{\mathcal{F}}$. It is possible using this concept without further limitations for

modelling the reversible adhesions, as exposed, e.g., by Maugis (2000). It is also possible to exploit this simple concept in case of fracture, by adding to the above minimization problem the irreversibility condition as a unilateral constraint applied on $\Delta\boldsymbol{\mathcal{F}}$. This technique has been adopted, for instance, by Kaczmarczyk et al., 2017. Notice that, differently from the classical variational approach adopted in Francfort et al. 2008, it isn't explicitly required any dissipative potential.

The static equilibrium can be calculated via a minimum principle only if the crack evolves at stable condition. In turn, the stability also depends on the boundary conditions. Actually, in many engineering applications, the stable crack propagation is realized by imposing the displacements of the loaded points via hard devices. However, even if the problem cannot be modelled as a stable one, it is possible, using the concept of arc-length (Riks, 1979), to evaluate the crack front at unstable equilibrium making stable the calculation algorithm. In essence, one introduces a fictious (not related to the physics) constraint among the degrees of freedom of the numerical model, and makes instead unknown the load parameter, be it related to the forces or the displacements. Dealing with the propagation problems, it is convenient to apply this fictious constraint to the area of the crack increment. In this way one will constraint directly the non-convex part of the problem, and this turns out to be the more efficient choice. We will apply such technique for the calculations presented in section 4.

In this section, the propagation will be considered stable for sake of simplicity. Hence, the load parameter λ is given, and the displacement field, as well as the crack front shape, represent the structure response in pursuing the minimum total free energy. More in detail, to get the unknowns $\Delta\boldsymbol{u}$, $\Delta\boldsymbol{\mathcal{F}}$ at equilibrium, one must solve for any given $\Delta\lambda$ the following constrained minimization problem:

$$\begin{cases} \min\limits_{\Delta\boldsymbol{u},\Delta\boldsymbol{\mathcal{F}}} \Pi(\boldsymbol{u_0},\lambda_0,\boldsymbol{\mathcal{F}}_0,\Delta\boldsymbol{u},\Delta\lambda,\Delta\boldsymbol{\mathcal{F}}) \\ \{\boldsymbol{S_0}\backslash\boldsymbol{\mathcal{F}_0}\} \cap \{\Delta\boldsymbol{S}\} = \emptyset \end{cases} \tag{3}$$

The constraint present in the above formulation establishes that no points of the crack surface increment, but the ones belonging to the crack front, can coincide with any point of the initial crack surface. This condition is equivalent to the irreversibility of the crack increment.

Assuming convex the elastic problem at fixed crack, the minimization (3) can be solved in two steps. First, calculate the minimum of Π for a varying $\Delta\boldsymbol{u}$ at each fixed $\Delta\boldsymbol{\mathcal{F}}$; second, minimize the result of the first operation respect to the variable $\Delta\boldsymbol{\mathcal{F}}$. Hence, as a first step, let's define the new free energy functional φ, corresponding to the minimum mechanical free energy at each fixed $\Delta\boldsymbol{\mathcal{F}}$.

$$\min_{\Delta\boldsymbol{u}} \phi(\boldsymbol{u_0}+\Delta\boldsymbol{u},\lambda_0+\Delta\lambda,\boldsymbol{\mathcal{F}}_0+\Delta\boldsymbol{\mathcal{F}}) = \varphi(\lambda_0+\Delta\lambda,\boldsymbol{\mathcal{F}}_0+\Delta\boldsymbol{\mathcal{F}}) \tag{4}$$

Notice that the functional (4) is uniquely defined also for nonlinear elastic problems. Thinking of the original Griffith model, the energy φ represents the share of elastic energy available for a generic crack increment. From now on, without loss of generality, the current crack front $\boldsymbol{\mathcal{F}}_0$, and the increment $\Delta\boldsymbol{\mathcal{F}}$ will be defined through a mapping in cylindrical coordinates. As depicted in figure 2, the polar axis is orthogonal to the crack plane, and the pole $\boldsymbol{O}$ location is the intersection between the two radial directions defining the emerging crack front points being parallel to the external surfaces, i.e.,

$$\boldsymbol{\mathcal{F}}_0 - \boldsymbol{O} = a_0(\theta)\boldsymbol{i}_\rho \tag{5}$$

Using this mapping, one can indicate the crack front points with a simple scalar equation: $\rho = a_0(\theta)$. Also the crack increment is easily indicated by the equation $\Delta\rho = \Delta a(\theta)$. Of course, as suggested in fig. 2, many different analytical representations of the crack front are equally licit. Indeed, the representation in cylindrical coordinates makes uniformly distributed the angular difference between the external surfaces, and this occurrence provides some interesting computational benefits, as will be shown in section 3.

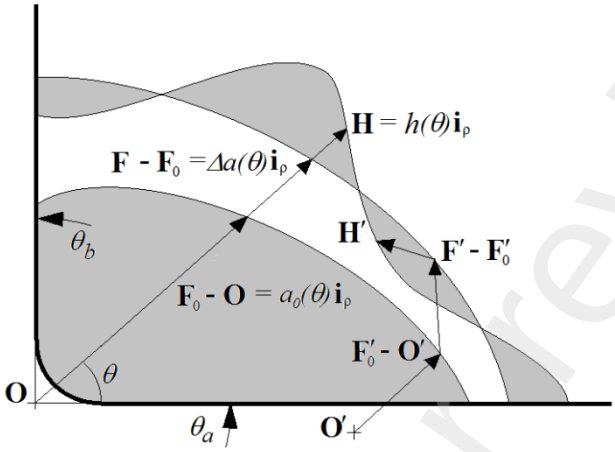

Figure 2 – Mapping of the initial crack front, the crack increment under testing and the virtual crack increment, in cylindrical coordinates or with generically oriented vectors.

Using the definition (4) and the above mapping, one can express the minimization problem (3) in the following simpler form:

$$\begin{cases} \min\limits_{\Delta a}\{\varphi(\lambda_0 + \Delta\lambda, a_0(\theta) + \Delta a(\theta)) + \mathcal{E}(a_0(\theta), \Delta a(\theta))\} \\ \Delta a(\theta) \geq 0 \quad \forall\theta \in [\theta_a, \theta_b] \end{cases} \tag{6}$$

To solve the problem (6), the following functional $\mathcal{L}$ is defined, where $\eta(\theta)$ is a Lagrange multiplier and $y^2(\theta)$ is an auxiliary nonnegative function allowing to impose the unilateral constraint (6_2):

$$\mathcal{L} = \varphi(\lambda_0 + \Delta\lambda, a_0(\theta) + \Delta a(\theta)) + \mathcal{E}(a_0(\theta), \Delta a(\theta)) + \eta(\theta)[\Delta a(\theta) - y^2(\theta)] \tag{7}$$

The necessary condition to the minimization (6) with the unknown function $\Delta a(\theta)$ states that the variations of the Lagrangian functional $\mathcal{L}$ with respect to the unknown functions $\Delta a, \eta, y$ must be zero. Formally:

$$\begin{aligned} &\lim_{\varepsilon\to 0}\frac{1}{\varepsilon}[\mathcal{L}(\lambda_0 + \Delta\lambda, a_0(\theta) + \Delta a(\theta) + \varepsilon h(\theta), \eta(\theta), y(\theta)) - \mathcal{L}(\lambda_0 + \Delta\lambda, a_0(\theta) + \Delta a(\theta), \eta(\theta), y(\theta))] = \\ &\lim_{\varepsilon\to 0}\frac{1}{\varepsilon}[\varphi(\lambda_0 + \Delta\lambda, a_0(\theta) + \Delta a(\theta) + \varepsilon h(\theta)) - \varphi(\lambda_0 + \Delta\lambda, a_0(\theta) + \Delta a(\theta))] + \\ &\lim_{\varepsilon\to 0}\frac{1}{\varepsilon}[\mathcal{E}(a_0(\theta), \Delta a(\theta) + \varepsilon h(\theta)) - \mathcal{E}(a_0(\theta), \Delta a(\theta))] + \eta(\theta)h(\theta) = 0 \qquad \forall h(\theta) \end{aligned} \tag{8a}$$

$$\lim_{\varepsilon\to 0}\frac{1}{\varepsilon}\left[\mathcal{L}(\lambda_0+\Delta\lambda,a_0(\theta)+\Delta a(\theta),\eta(\theta)+\varepsilon q(\theta),y(\theta))-\mathcal{L}(\lambda_0+\Delta\lambda,a_0(\theta)+\Delta a(\theta),\eta(\theta),y(\theta))\right]=q(\theta)$$
$$\left[\Delta a(\theta)-y^2(\theta)\right]=0 \qquad \forall q(\theta) \tag{8b}$$

$$\lim_{\varepsilon\to 0}\frac{1}{\varepsilon}\left[\mathcal{L}(\lambda_0+\Delta\lambda,a_0(\theta)+\Delta a(\theta),\eta(\theta),y(\theta)+\varepsilon p(\theta))-\mathcal{L}(\lambda_0+\Delta\lambda,a_0(\theta)+\Delta a(\theta),\eta(\theta),y(\theta))\right]=-2\eta(\theta)y$$
$$(\theta)p(\theta)=0 \qquad \forall p(\theta) \tag{8c}$$

In equation (8a) is present the variation of the functional φ, representing the opposite of the mechanical free energy released for a virtual crack increment $h(\theta)$, calculated at first order. From now on, it will be indicated with $\mathcal{G}$:

$$\mathcal{G}(\lambda_0+\Delta\lambda,a_0(\theta)+\Delta a(\theta),h(\theta))=-$$
$$\lim_{\varepsilon\to 0}\frac{1}{\varepsilon}\left[\varphi(\lambda_0+\Delta\lambda,a_0(\theta)+\Delta a(\theta)+\varepsilon h(\theta))-\varphi(\lambda_0+\Delta\lambda,a_0(\theta)+\Delta a(\theta))\right] \tag{9}$$

Notice that the functional $\mathcal{G}$ has the dimension of an energy. Hence, it is not to be confused with the energy release rate, which instead has the dimension of an energy to area ratio. In section 3 it will be shown in detail that $\mathcal{G}$ can be represented in the following form:

$$\mathcal{G}(\lambda_0+\Delta\lambda,a_0(\theta)+\Delta a(\theta),h(\theta))=\int_{\theta_a}^{\theta_b}\mathcal{C}(\lambda_0+\Delta\lambda,a_0(\theta)+\Delta a(\theta),\vartheta)h(\vartheta)a(\vartheta)d\vartheta \tag{10}$$

The functional $\mathcal{C}$ present in equation (10) has the dimension of an energy to area ratio and is defined at each point of the crack front (which, due to the mapping (5) are individuated by their coordinate ϑ). It depends on the crack front shape $\Delta a(\theta)$ and on the load parameter $\Delta\lambda$.

In equation (8a) is also present the variation of the fracture energy $\mathcal{E}$. If one assumes that it be proportional to the area of the crack increment and be independent on the crack front location within the volume domain, the unitary fracture energy will be a material property, and can be expressed with a unique scalar parameter J_c. Hence, the fracture energy variation is given by:

$$\mathcal{E}(a_0(\theta),\Delta a(\theta))=J_c\int_{\theta_a}^{\theta_b}\int_{a_0(\vartheta)}^{a(\vartheta)}\rho d\rho d\vartheta\Rightarrow\lim_{\varepsilon\to 0}\frac{1}{\varepsilon}\left[\mathcal{E}(a_0(\theta),\Delta a(\theta)+\varepsilon h(\theta))-\mathcal{E}(a_0(\theta),\Delta a(\theta))\right]=J_c$$
$$\int_{\theta_a}^{\theta_b}d\vartheta\lim_{\varepsilon\to 0}\frac{1}{\varepsilon}\int_{a(\vartheta)}^{a(\vartheta)+\varepsilon h(\vartheta)}\rho d\rho=J_c\int_{\theta_a}^{\theta_b}h(\vartheta)a(\vartheta)d\vartheta \tag{11}$$

Then, the necessary minimization condition (8a) is simplified as follows:

$$\int_{\theta_a}^{\theta_b}\mathcal{C}(\lambda_0+\Delta\lambda,a_0(\theta)+\Delta a(\theta),\vartheta)h(\vartheta)a(\vartheta)d\vartheta-J_c\int_{\theta_a}^{\theta_b}h(\vartheta)a(\vartheta)d\vartheta-\eta(\theta)h(\theta)=0 \qquad \forall h \tag{12}$$

It is possible to put under the integral also the third term of equation (12). To this aim, one can take advantage from the Dirac distribution $\delta(\vartheta,\theta)$ and rewriting the equation in weak form:

$$\int_{\theta_a}^{\theta_b}\left[\mathcal{C}(\lambda_0+\Delta\lambda,a_0(\theta)+\Delta a(\theta),\vartheta)a(\vartheta)-J_c a(\vartheta)-\delta(\vartheta,\theta)\eta(\theta)\right]h(\vartheta)d\vartheta=0 \qquad \forall h \tag{13}$$

Then, the test function *h* can be eliminated from equation (13) and the following pointwise condition is derived:

$$\mathcal{C}(\lambda_0 + \Delta\lambda, a_0(\vartheta) + \Delta a(\vartheta), \theta)a(\theta) - J_c a(\theta) - \eta(\theta) = 0 \qquad \forall\theta \tag{14}$$

On the other hand, combining the minimization conditions (8b), (8c) allows eliminating from the problem the auxiliary function $y^2(\theta)$. By this manipulation, one can derive a condition involving only the two functions $\Delta a(\theta)$, $\eta(\theta)$, that is:

$$\begin{cases} \Delta a(\theta) - y^2(\theta) = 0 \\ \eta(\theta) y(\theta) = 0 \end{cases} \Rightarrow \begin{cases} \Delta a(\theta)\eta(\theta) = 0 \\ \Delta a(\theta) \geq 0 \end{cases} \tag{15}$$

Next, the Lagrange multiplier $\eta(\theta)$ can also be eliminated by combining the equations (14), (15). This further manipulation transforms the minimization (necessary) condition (3) into a straightforward system of equations involving the functional $\mathcal{C}$ and the unknown crack front shape Δa, that is:

$$\begin{cases} [\mathcal{C}(\lambda_0 + \Delta\lambda, a_0(\vartheta) + \Delta a(\vartheta), \theta) - J_c]\Delta a(\theta) = 0 \\ \mathcal{C}(\lambda_0 + \Delta\lambda, a_0(\vartheta) + \Delta a(\vartheta), \theta) \leq J_c \\ \Delta a(\theta) \geq 0 \end{cases} \tag{16}$$

Clearly, the conditions (16) are the functional version of the well-known Kuhn-Tucker algebraic conditions (Kuhn and Tucker, 1951). Finally, formulas (16) can be further simplified, to get the following:

$$\begin{cases} \mathcal{C}(\lambda_0 + \Delta\lambda, a_0(\vartheta) + \Delta a(\vartheta), \theta) = J_c \quad if \;\; \Delta a(\theta) > 0 \\ \mathcal{C}(\lambda_0 + \Delta\lambda, a_0(\vartheta) + \Delta a(\vartheta), \theta) \leq J_c \quad if \;\; \Delta a(\theta) = 0 \end{cases} \tag{17}$$

The equations (17) represent the equilibrium condition of the crack front for a given load multiplier. In particular, the two equations state that the crack increment $\Delta a(\theta)$ is at equilibrium with $\Delta\lambda$ if the functional $\mathcal{C}(\theta)$ equates the fracture energy J_c at the crack front points where $\Delta a(\theta) > 0$, whereas, at the crack front points where $\Delta a(\theta) = 0$, $\mathcal{C}(\theta)$ is not higher than the fracture energy. It is worth recalling that the condition (17) doesn't imply the minimum of the functional Π, but represents only a necessary condition for it. Hence, such condition doesn't imply the stability of the equilibrium.

Apparently, the functional $\mathcal{C}(\theta)$ is like the pointwise energy release rate (see e.g., Li et al, 1985) or to the distributed configurational force (Gurtin and Podio-Guidugli, 1996). Hence, the condition (17) can also be interpreted as a three-dimensional extension of the Griffith criterion. More precisely, since the definition of the functional $\mathcal{C}(\theta)$ is not related to a virtual crack increment necessarily orthogonal to the front, it is more general of the pointwise energy release rate as usually defined in literature (see, e.g., Moran and Shih, 1987).

Also notice that the term 'configurational force' implicitly remands to a 'pushing direction' of the crack front and this idea is, in this author opinion, misleading. For this reason, in this work the functional $\mathcal{C}$ is named '(unitary) fracture potential'; the comparison with the (unitary) fracture energy J_c follows naturally. This point of view will be discussed in detail in section 3.

3 – Energy release and fracture potential evaluations

In this section, the first order energy $\mathcal{G}(\lambda,a(\theta),h(\theta))$, released due to a virtual crack front increment $h(\theta)$, will be evaluated. Further, it will be shown to be eventually expressed as a function of the fracture potential $\mathcal{C}(\theta)$, as stated in formula (10).

The energy release, as defined in equation (9), is the first order increment of the mechanical free energy when the crack is incremented by $h(\theta)$ preserving the static equilibrium. Its evaluation for a general three-dimensional crack increment is a well-established literature topic. Many methodologies are known to this aim, e.g., the virtual crack extension (Li et al., 1985), the energy domain integrals (Moran and Shih, 1987), or the Theta method (Destuynder and Djaoua, 1981). The common concepts to all of them were introduced by John D. Eshelby (Eshelby, 1975); he found an efficient methodology for calculating the mechanical free energy increment as depending on the 'displacement' of a defect within the elastic domain. Such increment is expressed as a function of the energy-momentum tensor $\boldsymbol{P} = w\boldsymbol{I} - \nabla\boldsymbol{u}^T\boldsymbol{\sigma}$, introduced by the author itself.

Taking advantage of the original formulation by De Lorenzi (1982) or the better formalized one by Suo and Combescure (1992), and neglecting, for simplicity, the volume forces, and the surface forces acting on the crack plane, one can calculate the energy release as follows:

$$\mathcal{G}(\lambda_0 + \Delta\lambda,a_0(\theta) + \Delta a(\theta),h(\theta)) = -\int_\Omega \boldsymbol{P}^T{:}(\nabla\boldsymbol{H})^T dv = \int_\Omega (\boldsymbol{\sigma}^T\nabla\boldsymbol{u} - w\boldsymbol{I}){:}(\nabla\boldsymbol{H})^T dv \qquad (18)$$

In the above equation, $\boldsymbol{\sigma}$, $\boldsymbol{u}$ and w represent the solution of the elastic problem at fixed crack front, i.e., in $(\lambda_0 + \Delta\lambda,a_0(\theta) + \Delta a(\theta))$; $\boldsymbol{H}$ is a vector field on Ω, whose value on the crack front is $h(\theta)\boldsymbol{i}_\rho$, and whose normal to the external surface component is zero. With reference to fig. 2, the vector field $h(\theta)\boldsymbol{i}_\rho$ on $\boldsymbol{\mathcal{F}}$ represents a general virtual increment of the crack front, expressed in cylindrical coordinates.

It is worth emphasizing that the vector $h(\theta)\boldsymbol{i}_\rho$ doesn't indicates the virtual displacement of the crack front single points. Instead, it only defines one among the infinite possible representations of the virtual deformation of the cracked domain in the configurational (or material) space (see, e.g., Casal, 1978). Hence, to calculate the crack propagation, assuming a biunivocal mapping between the initial crack front points $\{\boldsymbol{\mathcal{F}}_0\}$ and the incremented crack front points $\{\boldsymbol{\mathcal{F}}_0 + \Delta\boldsymbol{\mathcal{F}}\}$ is totally unnecessary (see fig. 2).

In the current literature, this misconception is often underlying, if not explicitly assumed. Probably, it originated the interpretation of the crack propagation as the displacement of the crack front points. This point of view brings thinking that the crack front points be 'pushed' by a 'driving force' having a direction orthogonal to the crack front line. For instance, Moran and Shih (1987) or Li et al. (1985) uphold that the energy domain integral methodology is like the virtual crack extension technique, and both are related to the orthogonal to the front crack extension. In their works the authors explicitly refer to a crack front 'transported' to the incremented state, and in fact use some transport theorems relative to the physical space. Switching to the configurational mechanics, Gürses and Miehe (2009), or Kaczmarczyk et al., 2014, for maximizing the dissipative power, seems having 'carried' the configurational force into the physical space and coupled its direction with the crack increment 'direction'.

In contrast, rigorously following the stationarity concept, the crack increment at a given point haven't any directions. Instead, the crack increment is to be viewed as an omni-directional expansion of the crack surface starting from each point of the crack front, which is caused by the fracture potential $\mathcal{C}(\theta)$ overcoming the fracture energy J_c.

With these premises at hand, to properly exploit the definition (18), it is convenient to divide the volume Ω into three separated volumes Ω_{I}, Ω_{II}, Ω_{III}, as depicted in fig. 3. Further, let's define the vector field $\boldsymbol{H}$ as follows:

$$\begin{aligned} &\boldsymbol{H} = h(\theta)\boldsymbol{i}_\rho && in\ \Omega_I \\ &\boldsymbol{H} = f(\rho,\theta,z)h(\theta)\boldsymbol{i}_\rho && in\ \Omega_{II},\ f(\rho,\theta,z) = \begin{cases} 1\ in\ \partial\overline{\Omega_{II}}\cap\partial\overline{\Omega_I} \\ 0\ in\ \partial\overline{\Omega_{II}}\cap\partial\overline{\Omega_{III}} \end{cases} \\ &\boldsymbol{H} = \boldsymbol{0} && in\ \Omega_{III} \end{aligned} \tag{19}$$

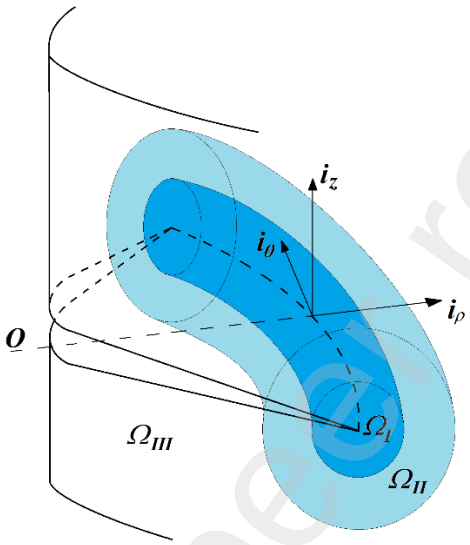

Figure 3 – Partition of the cracked domain into three sub-domains. Ω_{I} is the volume surrounding the crack front; Ω_{II}, the one surrounding Ω_{I}; Ω_{III} is the residual volume $\Omega\backslash(\Omega_{\mathrm{I}} \cup \Omega_{\mathrm{II}})$.

Applying the third of the conditions (19), formula (18) trivially provides:

$$\mathcal{G}_{\Omega_{III}} = 0 \tag{20}$$

The energy release share due to the volume Ω_{II} contribution can be evaluated using the integration by parts technique in formula (18). Since everywhere in Ω_{II} the stress field is smooth, it follows $div(\boldsymbol{P}^T) = \boldsymbol{0}$ (see Eshelby, 1975). Hence, it results:

$$\int_{\Omega_{II}} \boldsymbol{P}^T{:}(\nabla\boldsymbol{H})^T dv = \int_{\Omega_{II}} div(\boldsymbol{P}^T\boldsymbol{H})dv - \int_{\Omega_{II}} div(\boldsymbol{P}^T)\boldsymbol{H}dv = \int_{\Omega_{II}} div(\boldsymbol{P}^T\boldsymbol{H})dv \tag{21}$$

The divergence theorem, applied to formula (21), provides, being $\boldsymbol{N}$ the outgoing normal to the Ω_{II} boundary, the following result:

$$\mathcal{G}_{\Omega_{II}} = -\int_{\Omega_{II}} \boldsymbol{P}^T{:}(\nabla\boldsymbol{H})^T dv = -\int_{\partial\Omega_{II}} \boldsymbol{N}^T\boldsymbol{P}^T\boldsymbol{H}ds \tag{22}$$

With reference to fig. 4, the boundary of volume Ω_{II} is made by six surfaces S_k, i.e.,

$$\partial\Omega_{II} = \cup_{k=1}^{k=6} S_k \tag{23}$$

For these six surfaces, it results:

$$\begin{aligned} &\boldsymbol{H} = h(\theta)\boldsymbol{i}_\rho && on\ S_1 \\ &\boldsymbol{H} = \boldsymbol{0} && on\ S_2 \\ &\left.\begin{aligned} &\boldsymbol{\sigma N} = \boldsymbol{0} \\ &\boldsymbol{N}^T\boldsymbol{H} = 0 \end{aligned}\right\} && on\ S_3, S_4, S_5, S_6 \end{aligned} \tag{24}$$

Hence, the integrand function in eq. (22) gives zero on the surface S_2 because ***H*=0**, whereas on the surfaces S_3, S_4, S_5, S_6, the integrand function is null since it results:

$$\boldsymbol{N}^T\boldsymbol{P}^T\boldsymbol{H} = w\boldsymbol{N}^T\boldsymbol{H} - (\boldsymbol{\sigma N})^T\nabla\boldsymbol{u}\boldsymbol{H} = \boldsymbol{0} \tag{25}$$

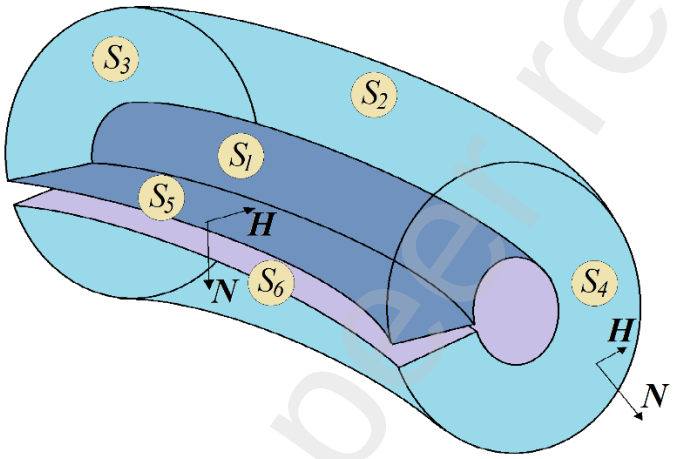

Figure 4. Representation of volume Ω_{II} with its boundary surfaces.

Therefore, the only nonzero contribution to the integral (22) is the one calculated on the surface S_1. Let's name ***n*=-*N*** the normal unitary vector outgoing to the volume Ω_I; finally, the energy release share due to the volume Ω_{II}, results the following:

$$\mathcal{G}_{\Omega_{II}} = \int_{S_1} \boldsymbol{n}^T\boldsymbol{P}^T\boldsymbol{i}_\rho h(\theta)ds \tag{26}$$

Further, considering again equations (18), (19), the energy release share due to the volume Ω_I, is given by:

$$\mathcal{G}_{\Omega_I} = -\int_{\Omega_I} \boldsymbol{P}^T{:}(\nabla(h(\theta)\boldsymbol{i}_\rho))^T dv \tag{27}$$

The equation (27) contains the gradient of the vector $h(\theta)\boldsymbol{i}_\rho$. In cylindrical coordinates, it gives:

$$\nabla(h(\theta)\boldsymbol{i}_\rho) = \begin{bmatrix} 0 & h_{,\theta}(\theta)/\rho & 0 \\ 0 & h(\theta)/\rho & 0 \\ 0 & 0 & 0 \end{bmatrix}_{(\rho,\theta,z)} \tag{28}$$

The subscript comma in the above matrix indicates the derivative with respect to the variable which follows it. Hence, the integrand function in equation (27) becomes:

$$-\boldsymbol{P}^T:(\nabla(h(\theta)\boldsymbol{i}_\rho))^T=\frac{1}{\rho}\Big[\boldsymbol{t}_\theta^T\frac{\partial\boldsymbol{u}}{\partial\rho}h_{,\theta}(\theta)+\Big(\boldsymbol{t}_\theta^T\frac{1}{\rho}\frac{\partial\boldsymbol{u}}{\partial\theta}-w\Big)h(\theta)\Big] \tag{29}$$

where:

$$\boldsymbol{t}_\theta=\boldsymbol{\sigma}\boldsymbol{i}_\theta=[\sigma_{\rho\theta},\sigma_{\theta\theta},\sigma_{z\theta}]^T \tag{30}$$

Finally, by assembling the contributions (20), (26), (27), and accounting for equation (29), one gets the energy release $\mathcal{G}$:

$$\mathcal{G}=\int_{S_1}\boldsymbol{n}^T\boldsymbol{P}^T\boldsymbol{i}_\rho h(\theta)ds+\int_{\Omega_I}\Big[\boldsymbol{t}_\theta^T\frac{\partial\boldsymbol{u}}{\partial\rho}h_{,\theta}(\theta)+\Big(\boldsymbol{t}_\theta^T\frac{1}{\rho}\frac{\partial\boldsymbol{u}}{\partial\theta}-w\Big)h(\theta)\Big]\frac{1}{\rho}dv \tag{31}$$

To the aim expressing the energy release as in equation (10), the virtual increment $h(\theta)$ must be evidenced. To do this, we are going to define an opportune mapping of the volume Ω_I and of the surface S_1. With reference to fig. 5, let consider a flat area D, lying in the plane (ρ, z), intersecting the crack front at the coordinate θ. Imagine translating this area D from the external surface ($\theta=\theta_a$) to the opposite one ($\theta=\theta_b$), by holding two conditions: first, D remains in the local plane (ρ, z) (i.e., remains orthogonal to $\boldsymbol{i}_\theta$); secondly, D intersects the crack front at a fixed point. With these rules, the volume Ω_I, the surface S_1 and their mapping are fully defined.

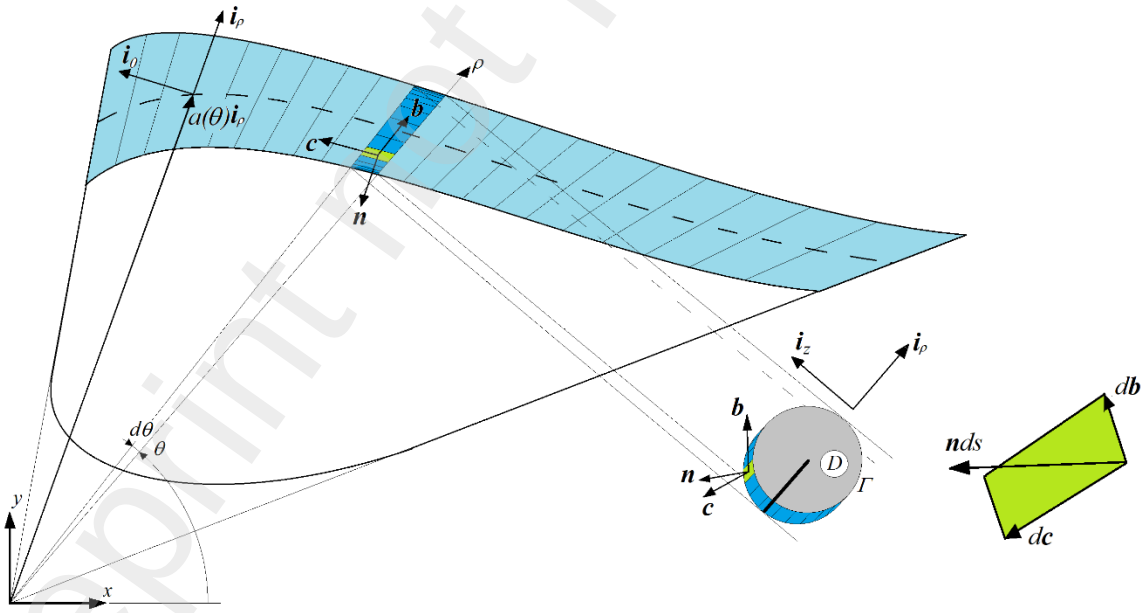

Figure 5 – Volume Ω_I with its cylindrical mapping.

Let consider the infinitesimal oriented element $d\boldsymbol{b}$ of the line $\Gamma=\partial D\backslash S$, which is the part of the D boundary not belonging to the crack surface. Let also consider the infinitesimal line element $d\boldsymbol{c}$, belonging to the surface S_1 and parallel to the crack front, as represented in fig. 5. These two infinitesimal vectors, together, define the infinitesimal area ds belonging to S_1 and its oriented normal unit vector $\boldsymbol{n}$. In details:

$$d\boldsymbol{b} = (b_\rho \boldsymbol{i}_\rho + b_z \boldsymbol{i}_z)dl \tag{32}$$

$$d\boldsymbol{c} = \left(\frac{a,_\theta(\theta)}{a(\theta)}\boldsymbol{i}_\rho + \boldsymbol{i}_\theta\right)\rho d\theta \tag{33}$$

$$\boldsymbol{n}ds = d\boldsymbol{b} \times d\boldsymbol{c} = (b_\rho \boldsymbol{i}_\rho + b_z \boldsymbol{i}_z) \times \left(\frac{a,_\theta(\theta)}{a(\theta)}\boldsymbol{i}_\rho + \boldsymbol{i}_\theta\right)\rho dl d\theta = \left(-b_z \boldsymbol{i}_\rho + b_\rho \boldsymbol{i}_z + \frac{a,_\theta(\theta)}{a(\theta)} b_z \boldsymbol{i}_\theta\right)\rho dl d\theta = \left(\boldsymbol{n}^{(D)} - \frac{a,_\theta(\theta)}{a(\theta)} n_\rho^{(D)} \boldsymbol{i}_\theta\right)\rho dl d\theta \tag{34}$$

In equation (34) the oriented elementary surface ***nds*** is split into two contributions. The first one, with direction $\boldsymbol{n}^{(D)}$, is parallel to the area *D* and orthogonal to its boundary Γ; the other one, is orthogonal to *D* or, equivalently, parallel to $\boldsymbol{i}_\theta$. Substituting the result (34) into the surface integral of equation (31), it gives:

$$\int_{S_1} \boldsymbol{n}^T \boldsymbol{P}^T \boldsymbol{i}_\rho h(\theta) ds = \int_{\theta_a}^{\theta_b} \int_{\Gamma(\theta)} \boldsymbol{i}_\rho^T \boldsymbol{P}\left(\boldsymbol{n}^{(D)} - \frac{a,_\theta(\theta)}{a(\theta)} n_\rho^{(D)} \boldsymbol{i}_\theta\right) h(\theta)\rho dl d\theta =$$
$$\int_{\theta_a}^{\theta_b} h(\theta)\left\{\int_{\Gamma(\theta)} \left(w n_\rho^{(D)} - \boldsymbol{t}_{\boldsymbol{n}^{(D)}}^T \frac{\partial \boldsymbol{u}}{\partial \rho}\right)\rho dl - \int_{\Gamma(\theta)} \frac{a,_\theta(\theta)}{a(\theta)} n_\rho^{(D)} \boldsymbol{t}_\theta^T \frac{\partial \boldsymbol{u}}{\partial \rho}\rho dl\right\} d\theta \tag{35}$$

Let define the line integrals I_{L1}, I_{L2} as follows:

$$I_{L1}(\theta) = \int_{\Gamma(\theta)} \left(w n_\rho^{(D)} - \boldsymbol{t}_{\boldsymbol{n}^{(D)}}^T \frac{\partial \boldsymbol{u}}{\partial \rho}\right)\rho dl; \quad I_{L2}(\theta) = -\frac{a,_\theta(\theta)}{a(\theta)} \int_{\Gamma(\theta)} n_\rho^{(D)} \boldsymbol{t}_\theta^T \frac{\partial \boldsymbol{u}}{\partial \rho}\rho dl \tag{36}$$

Formula (35) can now be written in the following, more compact, form:

$$\int_{S_1} \boldsymbol{n}^T \boldsymbol{P}^T \boldsymbol{i}_\rho h(\theta) ds = \int_{\theta_a}^{\theta_b} [I_{L1}(\theta) + I_{L2}(\theta)] h(\theta) d\theta \tag{37}$$

Then, let consider the volume integral of equation (31). Referring again to the notations reported in fig. 5, it results:

$$\int_{\Omega_l} \left[\boldsymbol{t}_\theta^T \frac{\partial \boldsymbol{u}}{\partial \rho} h,_\theta(\theta) + \left(\boldsymbol{t}_\theta^T \frac{\partial \boldsymbol{u}}{\partial \theta}\frac{1}{\rho} - w\right) h(\theta)\right]\frac{1}{\rho} dv =$$
$$\int_{\theta_a}^{\theta_b} h,_\theta(\theta)\left\{\int_{D(\theta)} \boldsymbol{t}_\theta^T \frac{\partial \boldsymbol{u}}{\partial \rho} ds\right\} d\theta + \int_{\theta_a}^{\theta_b} h(\theta)\left\{\int_{D(\theta)} \left(\boldsymbol{t}_\theta^T \frac{\partial \boldsymbol{u}}{\partial \theta}\frac{1}{\rho} - w\right) ds\right\} d\theta \tag{38}$$

Before operating on equation (38), it's useful defining the area integrals I_{SO}, I_{S1} as follows:

$$I_{SO}(\theta) = \int_{D(\theta)} \boldsymbol{t}_\theta^T \frac{\partial \boldsymbol{u}}{\partial \rho} ds; \; I_{S1}(\theta) = \int_{D(\theta)} \left(\boldsymbol{t}_\theta^T \frac{\partial \boldsymbol{u}}{\partial \theta}\frac{1}{\rho} - w\right) ds \tag{39}$$

To evidence the virtual crack increment *h(θ)* in the first integral of equation (38), one can apply to it the integration by parts.

$$\int_{\theta_a}^{\theta_b} h,_\theta(\theta) I_{SO}(\theta) d\theta = [h(\theta) I_{SO}(\theta)]_{\theta_a}^{\theta_b} - \int_{\theta_a}^{\theta_b} h(\theta) I_{SO,\theta}(\theta) d\theta \tag{40}$$

Since we assumed $\boldsymbol{t}_\theta = 0$ on the surfaces where the crack front emerges, it results:

$$[h(\theta)I_{SO}(\theta)]_{\theta_a}^{\theta_b} = 0 \tag{41}$$

It is worth noting that if the crack front line makes a loop within the volume domain, equation (41) is yet valid, since it results $\theta_b = \theta_a$.

In equation (40), the θ-derivative of the integral I_{SO} is present. Of course, the θ-derivative operates both on the integrand function and on its domain *D(θ)*. Nevertheless, since *D*, as a function of θ, is simply translated without any deformation, it is possible to operate the derivative inside the integral sign, by left unchanged *D(θ)*. This is attained by operating a directional derivative of the integrand function in the translation direction of each point of *D(θ)*. Actually, the translation corresponding to $d\theta$ of each point of *D* when it changes from *D(θ)* to *D(θ+dθ)* was already defined in formula (33) and depicted in fig. 5; it corresponds to the vector $d\boldsymbol{c} = dc_\rho \boldsymbol{i}_\rho + dc_\theta \boldsymbol{i}_\theta$. Hence, it results:

$$I_{SO,\theta}(\theta) = \frac{d}{d\theta}\int_{D(\theta)} \boldsymbol{t}_\theta^T \frac{\partial \boldsymbol{u}}{\partial \rho} ds = \int_{D(\theta)} \frac{d\boldsymbol{c}}{d\theta} \cdot \nabla\left(\boldsymbol{t}_\theta^T \frac{\partial \boldsymbol{u}}{\partial \rho}\right) ds = \int_{D(\theta)} \left[\frac{dc_\rho}{d\theta}\frac{\partial}{\partial \rho} + \frac{dc_\theta}{d\theta}\frac{1}{\rho}\frac{\partial}{\partial \theta}\right]\left(\boldsymbol{t}_\theta^T \frac{\partial \boldsymbol{u}}{\partial \rho}\right) ds \tag{42}$$

The $\boldsymbol{c}$ derivative to θ is easily recovered from equation (33); substituting it in equation (42), one gets $I_{SO,\theta}$ as a sum of two area integrals I_{S2}, I_{S3}, defined in the following expression:

$$I_{SO,\theta}(\theta) = \int_{D(\theta)} \frac{\partial}{\partial \theta}\left(\boldsymbol{t}_\theta^T \frac{\partial \boldsymbol{u}}{\partial \rho}\right) ds + \frac{a,_\theta(\theta)}{a(\theta)} \int_{D(\theta)} \frac{\partial}{\partial \rho}\left(\boldsymbol{t}_\theta^T \frac{\partial \boldsymbol{u}}{\partial \rho}\right) \rho ds = -I_{S2}(\theta) - I_{S3}(\theta) \tag{43}$$

Finally, assembling the results (37) to (43), the energy release (31) becomes:

$$\mathcal{G} = \int_{\theta_a}^{\theta_b} [I_{L1}(\theta) + I_{L2}(\theta) + I_{S1}(\theta) + I_{S2}(\theta) + I_{S3}(\theta)] h(\theta) d\theta \tag{44}$$

The comparison of equation (10) with the above one (44), confirms that the energy release can be calculated by integrating the fracture potential $\mathcal{C}(\theta)$ with the corresponding virtual crack increment $dA = h(\theta)a(\theta)d\theta$, as assumed in section 2, being the fracture potential defined by:

$$\mathcal{C}(\theta) = \frac{1}{a(\theta)}[I_{L1}(\theta) + I_{L2}(\theta) + I_{S1}(\theta) + I_{S2}(\theta) + I_{S3}(\theta)] \tag{45}$$

For the sake of simplicity, from now on, we will assume the static problem at fixed crack to be linear elastic; hence, the fracture potential turns out to be proportional to the square of the load parameter λ. Therefore, it is convenient to calculate it at a reference load level λ_0, so that the load parameter increment can be considered separately from $\mathcal{C}$:

$$\mathcal{C}(\lambda_0 + \Delta\lambda, a_0(\vartheta) + \Delta a(\vartheta), \theta) = \left(1 + \frac{\Delta\lambda}{\lambda_0}\right)^2 \mathcal{C}(\lambda_0, a_0(\vartheta) + \Delta a(\vartheta), \theta) \tag{46}$$

To sum up, the equilibrium condition between the load increment $\Delta\lambda$ and the crack front increment Δa, becomes:

$$\begin{cases}\left(1+\frac{\Delta\lambda}{\lambda_0}\right)^2\mathcal{C}(\lambda_0,a_0(\vartheta)+\Delta a(\vartheta),\theta)=J_c & if\ \ \Delta a(\theta)>0\\ \left(1+\frac{\Delta\lambda}{\lambda_0}\right)^2\mathcal{C}(\lambda_0,a_0(\vartheta)+\Delta a(\vartheta),\theta)\le J_c & if\ \ \Delta a(\theta)=0\end{cases} \tag{47}$$

where the fracture potential is given by the following sum:

$$\mathcal{C}(\lambda_0,a(\vartheta),\theta)=J_{L1}^{cyl}(\theta)+J_{L2}^{cyl}(\theta)+J_{S1}^{cyl}(\theta)+J_{S2}^{cyl}(\theta)+J_{S3}^{cyl}(\theta) \tag{48}$$

whose terms are given by the following expressions:

$$J_{L1}^{cyl}(\theta)=\frac{1}{a(\theta)}\int_{\Gamma(\theta)}\left(wn_\rho^{(D)}-\boldsymbol{t}_{\boldsymbol{n}^{(D)}}^T\frac{\partial\boldsymbol{u}}{\partial\rho}\right)\rho dl \tag{49a}$$

$$J_{L2}^{cyl}(\theta)=-\frac{a_{,\theta}(\theta)}{a^2(\theta)}\int_{\Gamma(\theta)}n_\rho^{(D)}\boldsymbol{t}_\theta^T\frac{\partial\boldsymbol{u}}{\partial\rho}\rho dl \tag{49b}$$

$$J_{S1}^{cyl}(\theta)=-\frac{1}{a(\theta)}\int_{D(\theta)}\left(w-\boldsymbol{t}_\theta^T\frac{\partial\boldsymbol{u}}{\partial\theta}\frac{1}{\rho}\right)ds \tag{49c}$$

$$J_{S2}^{cyl}(\theta)=-\frac{1}{a(\theta)}\int_{D(\theta)}\frac{\partial}{\partial\theta}\left(\boldsymbol{t}_\theta^T\frac{\partial\boldsymbol{u}}{\partial\rho}\right)ds \tag{49d}$$

$$J_{S3}^{cyl}(\theta)=-\frac{a_{,\theta}(\theta)}{a^2(\theta)}\int_{D(\theta)}\frac{\partial}{\partial\rho}\left(\boldsymbol{t}_\theta^T\frac{\partial\boldsymbol{u}}{\partial\rho}\right)\rho ds \tag{49e}$$

In equations (49), the terms $\boldsymbol{u}$, w and $\boldsymbol{t}$ represent the static solution calculated at $\lambda = \lambda_o$, $a(\theta) = a_0(\theta) + \Delta a(\theta)$. The fracture potential (48) describes the pointwise 'tension' acting on the crack front. It is composed by the sum of two line integrals and three surface integrals, respectively calculated on the domains $\Gamma(\theta)$, $D(\theta)$, which are located and oriented following the global cylindrical reference frame of fig. 5.

Using different calculation techniques, like the virtual crack extension method (Moran and Shih, 1987) or the Theta method (Destuynder and Djaoua, 1981), similar, but less general, results can be also achieved. Compared to these well-established methodologies, the innovative aspect of the result (47 ÷ 49) consists of the possibility to calculate the integrals (49) on domains non orthogonal to the crack front. By this property, calculating the fracture potential (which, in this context, is the equivalent of the pointwise energy release rate) in the neighbourhood of the external surfaces turns out to be easy and accurate like in any other point of the crack front.

Discussion and particularizations

The fracture potential is evaluated, at each point θ of the crack front, by using displacements, stresses, and their derivatives of the corresponding two-dimensional domain $D(\theta)$. Since $D(\theta)$ can be chosen arbitrarily small, $\mathcal{C}(\theta)$ actually depends on quantities arbitrarily close to θ; this makes it, in fact, a local parameter. Therefore, it is also licit to map the volume Ω_I, in the neighbourhood of θ, using some local coordinate system, defined for merely computational convenience. In fig. 6, four different local mappings/reference frames of the volume Ω_I are depicted. Them generate as many particularizations of the integrals composing the fracture potential.

The mapping (a) is the one utilized so far, which gives, of course, the five integrals (49a ÷ 49e). It is also the unique mapping suitably describing the whole volume with a unique reference frame.

The mapping (b) can be obtained by degenerating the cylindrical reference frame (ρ, θ, z) into a cartesian one (x, y, z), whose x direction is arbitrarily rotated about z. The corresponding integrals can be obtained by assuming in the formulas (49) $\rho \to +\infty$, $\rho d\theta \to dy$. It's easy to verify that this position implies $J_{S1}^{car}(y) = 0$; the remaining four integrals become:

$$J_{L1}^{car}(y) = \int_{\Gamma(y)} \left(w n_x^{(D)} - \boldsymbol{t}_{\boldsymbol{n}^{(D)}}^T \frac{\partial \boldsymbol{u}}{\partial x} \right) dl \quad (50a)$$

$$J_{L2}^{car}(y) = -a_{,y}(y) \int_{\Gamma(y)} n_x^{(D)} \boldsymbol{t}_y^T \frac{\partial \boldsymbol{u}}{\partial x} \, dl \quad (50b)$$

$$J_{S2}^{car}(y) = -\int_{D(y)} \frac{\partial}{\partial y} \left(\boldsymbol{t}_y^T \frac{\partial \boldsymbol{u}}{\partial x} \right) ds \quad (50c)$$

$$J_{S3}^{car}(y) = -a_{,y}(y) \int_{D(y)} \frac{\partial}{\partial x} \left(\boldsymbol{t}_y^T \frac{\partial \boldsymbol{u}}{\partial x} \right) ds \quad (50d)$$

It is worth noting that the line integral (50a) corresponds to the Rice J-integral calculated on the (x, z) plane, which is in general non orthogonal to the crack front. Further, the surface integral (50c) corresponds to the contribution pointed out, e.g., by Amestoy et al., 1981. The remaining integrals (50b) and (50d) depend on the angle between the crack front and the domain *D(y)*; in our best knowledge, they have been introduced for the first time in this work.

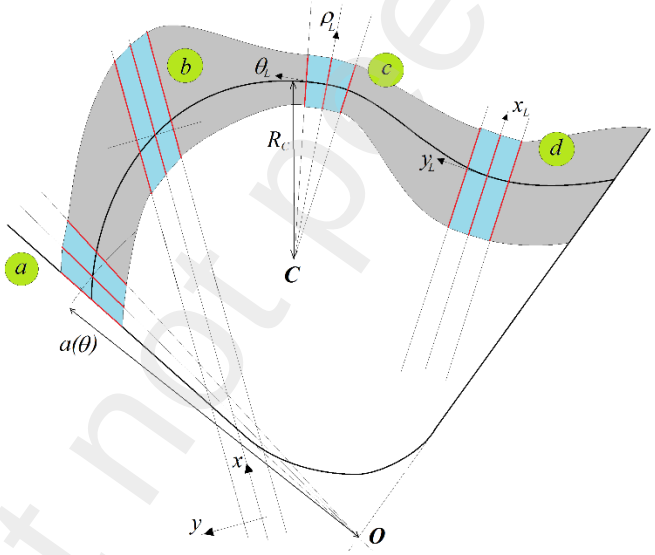

Figure 6 – Mapping of Ω_I. (a): global cylindrical, which is the only one generally valid at the whole crack front. (b): global cartesian with arbitrary *x, y* orientation. (c): local orthogonal cylindrical. (d): local orthogonal cartesian.

The mapping (c) corresponds to a local curvilinear reference frame, whose radial axis is orthogonal to the crack front and whose radius of curvature $R_c(\theta)$ corresponds to its local curvature. In this case, the derivatives $a_{,\theta}$ are null; hence, it results $J_{L2}^{cyl,\,ort} = J_{S3}^{cyl,\,ort} = 0$. The remaining three integrals become:

$$J_{L1}^{cyl,\,ort}(\theta) = \frac{1}{R_c(\theta)} \int_{\Gamma(\theta)} \left(w n_\rho^{(D)} - \boldsymbol{t}_{\boldsymbol{n}^{(D)}}^T \frac{\partial \boldsymbol{u}}{\partial \rho} \right) \rho \, dl \quad (51a)$$

$$J_{S1}^{cyl,\,ort}(\theta) = -\frac{1}{R_c(\theta)} \int_{D(\theta)} \left(w - \boldsymbol{t}_\theta^T \frac{\partial \boldsymbol{u}}{\partial \theta} \frac{1}{\rho} \right) ds \quad (51b)$$

$$J_{S2}^{cyl,\,ort}(\theta) = -\frac{1}{R_c(\theta)} \int_{D(\theta)} \frac{\partial}{\partial \theta} \left(\boldsymbol{t}_\theta^T \frac{\partial \boldsymbol{u}}{\partial \rho} \right) ds \quad (51c)$$

This evaluation of the fracture potential coincides with the result obtained e.g., by Eriksonn, 2002.

Finally, the mapping (d) corresponds to the more common local cartesian reference frame, whose *x* axis is orthogonal to the crack front, as reported, e.g., by Amestoy et al (1981) or Giner et al. (2010). In this case, it results $J_{L2}^{car,\,ort} = J_{S2}^{car,\,ort} = J_{S3}^{car,\,ort} = 0$. The remaining two integrals provide the following well-known fracture potential:

$$\mathcal{C}(\lambda_0, a(v), y) = \int_{\Gamma(y)} \left(wn_x^{(D)} - \boldsymbol{t}_{\boldsymbol{n}^{(D)}}^T \frac{\partial \boldsymbol{u}}{\partial x} \right) dl - \int_{D(y)} \frac{\partial}{\partial y} \left(\boldsymbol{t}_y^T \frac{\partial \boldsymbol{u}}{\partial x} \right) ds \tag{52}$$

It's easily verified that, since the singularity of the integrand functions is weaker than ρ^{-2}, when the area of the domain *D* approaches to zero, the area integrals J_{Si} tend to vanish. In these conditions, it also results $\rho(\theta) \rightarrow a(\theta)$; hence, the integrals (49) can be, in principle, evaluated as follows:

$$J_{L1}^{\varepsilon}(\theta) = \lim_{\Gamma \to 0} \int_{\Gamma(\theta)} \left(wn_\rho^{(D)} - \boldsymbol{t}_{\boldsymbol{n}^{(D)}}^T \frac{\partial \boldsymbol{u}}{\partial \rho} \right) dl \tag{53a}$$

$$J_{L2}^{\varepsilon}(\theta) = -\frac{a_{,\theta}(\theta)}{a(\theta)} \lim_{\Gamma \to 0} \int_{\Gamma(\theta)} n_\rho^{(D)} \boldsymbol{t}_\theta^T \frac{\partial \boldsymbol{u}}{\partial \rho}\, dl \tag{53b}$$

$$J_{S1}^{\varepsilon} = J_{S3}^{\varepsilon} = J_{S3}^{\varepsilon} = 0 \tag{53c}$$

Further, if equation (47) is calculated in a reference frame orthogonal to the crack front, let it be curvilinear or cartesian, it also results $J_{L2}^{\varepsilon} = 0$, and the fracture potential is given by the following expression:

$$\mathcal{C}(\lambda_0, a(\vartheta), \theta) = \lim_{\Gamma \to 0} \int_{\Gamma_{ort}(\theta)} \left(wn_\rho^{(D)} - \boldsymbol{t}_{\boldsymbol{n}^{(D)}}^T \frac{\partial \boldsymbol{u}}{\partial \rho} \right) dl \tag{54}$$

The expression (54) of the fracture potential coincides with the pointwise J-integral as defined, e.g., in Blackburn (1972). The major drawbacks of this formulation are well-known: first, due to the stress field singularity, the precision of the numerical evaluations is generally poor; second, it fails in the neighbourhood of the external surfaces, since in general it is $a_{,\theta}(\theta) \neq 0$. The more general formulation (53) fixes the latter problem, but not the former. On the other hand, using the formulations (49) ÷ (52), fixes the first problem. As previously highlighted, since the domain *D* is by construction parallel to the external surfaces, the expression (49) of the fracture potential naturally fixes both problems. In conclusion, it is confirmed that the fracture potential $\mathcal{C}$ is independent on any direction of the virtual configurational displacement ***H***.

From the analytical point of view, formulas (49) ÷ (54), where appliable, are all equivalent; from the computational point of view, they are not. For instance, using the boundary elements method, makes equally difficult calculating the fracture potential with anyone of the formulas (49) ÷ (52), since the volume mesh is not a priori fixed. In contrast, using the FE method, it is convenient to make the volume mesh so that the domains *D(θ)*, even if they were different each other, coincide with a meshed surface. In this case, using the general expressions (49), (50) allows for a notably more regular volume mesh.

Further, notice that the surface integrals J_{S2} and J_{S3} contain stress derivatives, whose suitable and accurate evaluation isn't easy to attain by numerical calculations. By arranging the volume mesh so that all

the domains *D(θ)* have the same shape, dimension and surface mesh, one can exploit the relation (43), which implies:

$$J_{S2}^{cyl}(\theta) + J_{S3}^{cyl}(\theta) = -\frac{1}{a(\theta)}\frac{d}{d\theta}\int_{D(\theta)} \boldsymbol{t}_\theta^T \frac{\partial \boldsymbol{u}}{\partial \rho}\, ds \qquad (55a)$$

$$J_{S2}^{car}(y) + J_{S3}^{car}(y) = -\frac{d}{dy}\int_{D(y)} \boldsymbol{t}_y^T \frac{\partial \boldsymbol{u}}{\partial x}\, ds \qquad (55b)$$

Contrarily to the expressions (49), (50), the integrand functions in the above equations (55) do not contain any second derivatives of displacements; In this form, the sum $J_{S2} + J_{S3}$ results much easier to calculate accurately. In fact, it can be directly performed by finite differences on the variables θ or *y* of the integrals in formulas (55), previously calculated.

It's worth highlighting that these results have been obtained taking advantage of the total free energy stationarity condition, without any further assumption. This general result is also valid for the mixed mode fracture, as long as the fracture energy J_c be mode-independent (as it should be, if the physics of fracture is accurately described as a creation of new surfaces, without irreversible volume changes). Further, it holds valid also if the material is nonlinear elastic, anisotropic, or in case of interface fracture.

4 – Evaluation of the crack front evolution

In the most part of the relevant literature, the quasi-static crack propagation is dealt by introducing some *ad hoc* crack increment criterion. For instance, Galdos (1997) calculated the local crack increment as the α-th power of the pointwise energy release rate, where the parameter α was considered a material property. Further, Kuhn and Müller (2010) faced the problem using a phase field model based on the configurational mechanics. These authors calculated the local crack increment via introducing a new material property (the so-called 'crack mobility'), which was defined to impose the maximum dissipation power. Gürses and Miehe (2009) also introduced a 'constitutive law' ruling the increment, which is conceptually like introducing the crack mobility. In particular, they defined the crack increment as proportional to the difference between the configurational force module and the energy fracture. Gurtin and Podio-Guidugli (1996) also adopted a similar approach.

In contrast to the aforecited works, in the present one the quasi-static crack propagation problem is solved without introducing any 'propagation criterion'. In fact, the crack increment is nothing more than the solution of the nonlinear functional equation (47), whose unknown is precisely Δa.

By means of equations (48), one can derive the fracture potential along the crack front at a fixed Δa. As for any nonlinear numerical problem, one must define a trial value for Δa to be iteratively substituted in the main equation until the convergence conditions are fulfilled; hence, some predictor for the trial value is also necessary. In this section, two different predictors will be introduced to this aim.

As an exemplification case, we calculated via FEM the crack front shape evolution of a symmetric isotropic double cantilever beam (DCB) specimen loaded in opening mode, as depicted in fig. 7. The volume Ω_I mesh was realized by translating along the crack front line, without rotations, a plane circular meshed area *D* parallel to the *xz* plane, holding the centre of *D* coincident with the crack front points. Since the external surfaces where the crack emerges are parallel each other, the general formulation (49) of the fracture potential degenerates into the integrals (50).

Further, we exploited the equation (55b), which is valid when the shape and the position relatively to the front of the domain *D(y)* are constant. Therefore, the fracture potential turns out to be the sum of three integrals J_{L1},J_{L2}, J'_{SO}, as specified in the following formula:

$$\mathcal{C}(y) = R\int_{-\pi}^{\pi}\left(w\cos\alpha - \boldsymbol{t}_{\boldsymbol{n}^{(D)}}^{T}\frac{\partial \boldsymbol{u}}{\partial x}\right)d\alpha - a_{,y}(y)R\int_{-\pi}^{\pi}\boldsymbol{t}_{y}^{T}\frac{\partial \boldsymbol{u}}{\partial x}\cos\alpha d\alpha - \frac{d}{dy}\int_{-\pi}^{\pi}d\alpha\int_{0}^{R}\left(\boldsymbol{t}_{y}^{T}\frac{\partial \boldsymbol{u}}{\partial x}\right)rdr \qquad (56)$$

As shown in fig. 7, the volume Ω_I was meshed very accurately, having 50 layers of elements along the width B and about 16000 esaedric elements in total. Since we exploited the double symmetry, the volume really processed was only a quarter of Ω_I (25 layers and about 4000 elements). The fracture potential was calculated at each of the *n* = 26 surfaces $D(y_i)$.

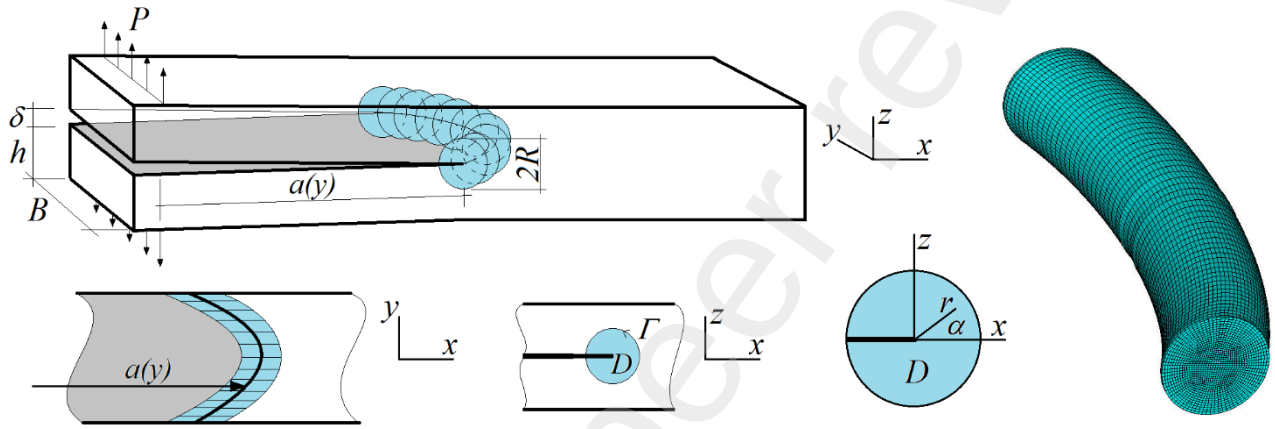

Figure 7. DCB model used for calculating the crack front evolution. The relevant dimensions are B=20; h=10; R=2; Material properties: E=72000; ν=0.35.

The opening displacement δ was applied to this model. As well known, these boundary conditions on the DCB geometry make the crack propagation stable. However, for the sake of computational efficiency, it is convenient imposing the crack surface increment ΔA and leaving unknown the load parameter increment $\Delta\lambda$, which is applied here to the opening displacement δ (see discussion on the Riks' algorithm in sec. 2). Further, we assumed for simplicity that at the first equilibrium step the crack front was already fully developed, so that only the first of the two equations (47) was actually involved in the calculations of the crack front evolution.

At each iteration, an updated crack front and a new mesh were automatically realized by means of a APDL script, running with the commercial FE software ANSYS. Once the current elastic problem has run, in the postprocessing phase another APDL script allows calculating the current fracture potentials (56). Then, by means of a predictor algorithm, the new trial crack front model is realized, and the cycle goes on until the convergence criterion is fulfilled.

It is worth emphasizing that, thanks to the formulation (56), one can realize a quite regular mesh, unrelated to the orthogonality to the crack front, particularly near the external surfaces. In contrast, in most of the relevant literature, the unnecessary condition of the orthogonal to the front crack propagation, forces defining there a very poor mesh (see, e.g., Oplt et al., 2019). As a result, a spurious boundary effect on the crack front shape has been occasionally reported.

We calculated the crack front evolution using two different numerical techniques: the former, is based on the direct application of equation (47) in discretized form; the latter, is a variational technique, based on the weak form of the same equation.

Strong form solution

The strong form numerical solution was pointed out by applying the first of equations (47) in all the *n* points y_i of the meshed crack front, corresponding to the plane domains $D(y_j)$ on which the integrals (56) are calculated. Let it be $a_i = a(y_i)$ and let ΔA be the imposed area increment of the crack surface; further, let q_i be opportune weight factors for the surface numerical integration. The set of equations arising from the previous definitions is the following:

$$\left(1+\frac{\Delta\lambda}{\lambda_0}\right)^2 \mathcal{C}(\lambda_0,\{a_i\},y_1) = J_c \qquad (57a)$$

$$\mathcal{C}(\lambda_0,\{a_i\},y_j) = \mathcal{C}(\lambda_0,\{a_i\},y_1), \qquad j = 2,\dots,n \qquad (57b)$$

$$\int_{y_a}^{y_b} \Delta a(y)dy = \Delta A \rightarrow \sum_{i=1}^{n} (a_i - a_{0i})q_i = \Delta A \qquad (57c)$$

In details, the equation (57c) defines the total area of the crack increment; the equation (57b) requires the fracture potential to be constant along the crack front; the equation (57a) imposes the equilibrium condition between the fracture energy J_c and the load increment $\Delta\lambda$.

The system of equations (57b), which is independent on $\Delta\lambda$, must be solved iteratively. The first trial value of the unknown a_i is calculated as the uniform increment of the crack front which area is ΔA; it is easily provided by equation (57c):

$$a_i^1 = a_{0i} + \frac{\Delta A}{\sum_{j=1}^{n} q_j} \qquad (58)$$

The next trials are provided by an *ad hoc* predictor for the equation (57b); it gives trial increments of a_i approximatively proportional to the current residual $\mathcal{C}(y_i) - J_c$ and corresponding to a null area increment, so that the total area of the crack increment remains unaltered over the iterations. The predictor is the following:

$$a_j^k = a_j^{k-1} + \gamma \sum_{h=1}^{n} \left(\delta_{jh} - \frac{q_h}{\sum_{r=1}^{n} q_r}\right)\left[\mathcal{C}\left(\lambda_0,\{a_i^{k-1}\},y_h\right) - \overline{\mathcal{C}}_{k-1}\right] \qquad (59)$$

$$\overline{\mathcal{C}}_{k-1} = \frac{1}{n}\sum_{h=1}^{n} \mathcal{C}\left(\lambda_0,\{a_i^{k-1}\},y_h\right)$$

In the above formula, δ_{jh} is the Kroneker Delta, and γ is a tuning parameter for stabilizing the algorithm. Once calculated the convergent solution of equations (57b), that is the crack front $\{a_i\}$, the equation (57a) finally provides the load parameter $\Delta\lambda$ as follows:

$$\Delta\lambda = \lambda_0\left(\sqrt{\frac{J_c}{\mathcal{C}(\lambda_0,\{a_i\},y_1)}} - 1\right) \qquad (60)$$

After few iterations, the trial crack front assumes a shape nearly convergent but, particularly near the external surfaces, the convergence becomes more and more slower. Actually, to obtain the requested convergence level, that was set as $max(\mathcal{C}(y_i) - J_c) \leq 0.001 J_c$, it needed about 200 iterations.

Weak form solution

To improve the computational efficiency, we also used a different strategy, which is based on imposing the equation (47) in weak form. The variational equation to be solved is the following:

$$\int_{y_a}^{y_b} \left[\left(1 + \frac{\Delta\lambda}{\lambda_0}\right)^2 \mathcal{C}(\lambda_0, a(v), y) - J_c \right] t(y) dy = 0 \qquad \forall t \tag{61}$$

Using the standard Galerkin solution technique, one seeks for an approximate value of the unknown *a(y)* by exploring a subspace defined through some shape functions $\beta_i(y)$, which also describe the test function *t(y)*; in detail:

$$a(y) = a_0(y) + p_i \beta_i(y) \qquad i = 1 \ldots m \tag{62a}$$

$$t(y) = q_i \beta_i(y) \qquad i = 1 \ldots m \tag{62b}$$

Further, without any loss of generality, the shape functions are required to respect the following conditions:

$$\beta_1(y) = 1; \quad \int_{y_a}^{y_b} \beta_i(y) dy = 0, \qquad i = 2, \ldots, m \tag{63}$$

Substituting the approximate forms (62) into the variational equation (61), a discrete nonlinear system of equations results, with the unknowns p_i, $\Delta\lambda$. Taking advantage of the condition (63), also in this case it results: a single equation, imposing the equilibrium condition between the fracture energy and the load increment, plus a separate system of equations, imposing the fracture potential to be constant along the crack front. The condition defining the total area of the crack increment has been added to these equations. In the end, the numerical problem consists of the following three separate equations:

$$\left(1 + \frac{\Delta\lambda}{\lambda_0}\right)^2 \int_{y_a}^{y_b} \mathcal{C}(\lambda_0, a_0(v) + p_i \beta_i(v), y) dy = J_c (y_b - y_a) \tag{64a}$$

$$\int_{y_a}^{y_b} \mathcal{C}(\lambda_0, a_0(v) + p_j \beta_j(v), y) \beta_i(y) dy = 0 \qquad i = 2, \ldots, m \tag{64b}$$

$$\int_{y_a}^{y_b} [a(y) - a_0(y)] dy = \Delta A \tag{64c}$$

Thanks to the conditions (63), the equation (64c) straightforwardly provides the first unknown p_1:

$$\Delta A = \int_{y_a}^{y_b} p_i \beta_i(y) dy = p_1 (y_b - y_a) \Longrightarrow p_1 = \frac{\Delta A}{(y_b - y_a)} \tag{65}$$

Then, the system of m-1 equations in the m-1 unknowns $p_2, \ldots, p_m$ (64b) has to be solved iteratively. Finally, the equation (64a) provides the load parameter $\Delta\lambda$ by the following formula:

$$\Delta\lambda = \lambda_0\left(\sqrt{\frac{J_c(y_b - y_a)}{\int_{y_a}^{y_b} \mathcal{C}(\lambda_0, a_0(v) + p_i\beta_i(v), y)dy}} - 1\right) \tag{66}$$

To solve the DCB problem, we chose as shape functions the even polynomials and *m*=3. Therefore, the general approximate form of the crack front turns out to be the following:

$$a(y) = a_0(y) + \frac{\Delta A}{(y_b - y_a)} + p_2\left[\left(\frac{y}{y_b - y_a}\right)^2 - \frac{1}{3}\right] + p_3\left[\left(\frac{y}{y_b - y_a}\right)^4 - \frac{1}{5}\right] \tag{67}$$

Using the approximation (67), the equation (64b) generates the following nonlinear system of two equations with the unknown variables p_2, p_3.

$$\begin{cases} \int_{y_a}^{y_b} \mathcal{C}(\lambda_0, a(v; p_2, p_3), y)\left[\left(\frac{y}{y_b - y_a}\right)^2 - \frac{1}{3}\right]dy = 0 \\ \int_{y_a}^{y_b} \mathcal{C}(\lambda_0, a(v; p_2, p_3), y)\left[\left(\frac{y}{y_b - y_a}\right)^4 - \frac{1}{5}\right]dy = 0 \end{cases} \tag{68}$$

The numerical integration required for calculating the terms of equation (68) was realized using the pointwise fracture potentials $\mathcal{C}(y_i)$ previously evaluated with the same mesh and at the same n = 26 points y_i as for the strong form solution (see eq. 57). As a predictor, the inverse of the gradient of equation (68) was used, approximately evaluated, at each iteration, by finite differences with respect to the variables p_2, p_3. More in detail, let (p_2^k, p_3^k) be the current value of the unknown variables; let also define:

$$f_i(p_2^k, p_3^k) = \int_{y_a}^{y_b} \mathcal{C}(\lambda_0, a_0(v) + p_j^k\beta_j(v), y)\beta_i(y)dy \tag{69}$$

The next approximation is given by the following formula:

$$\begin{bmatrix} p_2^{k+1} \\ p_3^{k+1} \end{bmatrix} = \begin{bmatrix} p_2^k \\ p_3^k \end{bmatrix} - \varepsilon\begin{bmatrix} f_2(p_2^k + \varepsilon, p_3^k) - f_2(p_2^k, p_3^k) & f_2(p_2^k, p_3^k + \varepsilon) - f_2(p_2^k, p_3^k) \\ f_3(p_2^k + \varepsilon, p_3^k) - f_3(p_2^k, p_3^k) & f_3(p_2^k, p_3^k + \varepsilon) - f_3(p_2^k, p_3^k) \end{bmatrix}^{-1}\begin{bmatrix} f_2(p_2^k, p_3^k) \\ f_3(p_2^k, p_3^k) \end{bmatrix} \tag{70}$$

Of course, this technique makes the convergence much faster. In fact, only 8 iterations (which require the stress field at fixed crack to be evaluated 16 times) are sufficient to attain the same accuracy provided by 200 iterations of the strong form algorithm. Such a difference is due both to the higher numerical stability of the second algorithm and to the different accuracy of the respective predictors.

Results of the simulations

In figs. 8 and 9 some results for a given load step are reported, corresponding to the opening displacement δ/h = 0.244 and to the load F/BJ_c=19.9. With these boundary conditions, the pointwise crack length *a(y)* (see fig. 7) is *a/h* = 6.43 at the external surfaces and *a/h* = 6.61 on the symmetry plane *xz*.

In fig. 8 the converged crack front shape is reported, and the results provided by the two calculation techniques described above are compared. It can be noted a small oscillation of the strong solution involving few points closer to the external surface. In contrast, as expected, the weak solution

provides a very smooth behaviour everywhere on the crack front. However, the two results are practically indistinguishable.

In fig. 9, the dimensionless convergent values of the integrals J_{L1}, J_{L2}, J'_{SO} and their sum, which is the fracture potential $\mathcal{C}(\lambda,a(\upsilon),y)$, are reported. As expected, the fracture potential turns out to be constant along the crack front within a precision range smaller than 1/1000. The line integral J_{L1} gives the main contribution to the fracture potential; it corresponds to the J-integral, calculated on planes parallel to the external surfaces. The second more large contribution turns out to be the derivative J'_{SO}, which is notable near the external boundary. Finally, the integral J_{L2} contributes, at its maximum (which is located at about B/10 from the external boundary), with about 1.5% of the total.

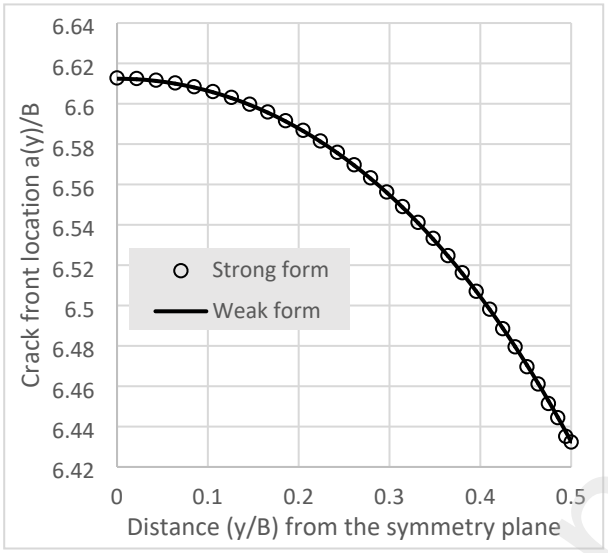

Figure 8 – DCB crack front shape.

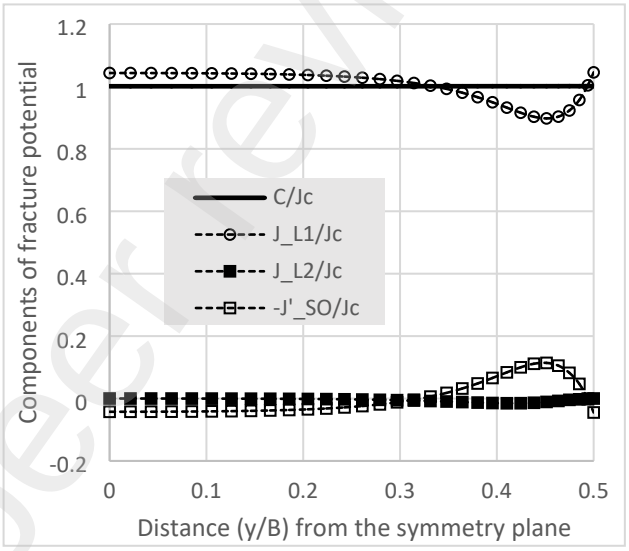

Figure 9 – Dimesionless components of the fracture potential.

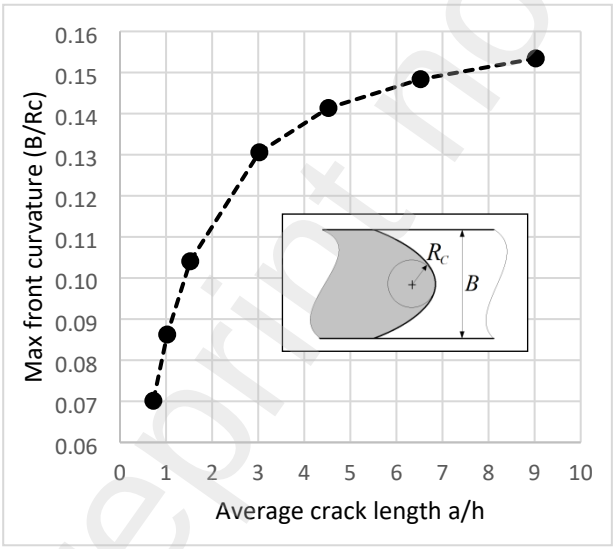

Figure 10 – Crack front curvature vs average crack length.

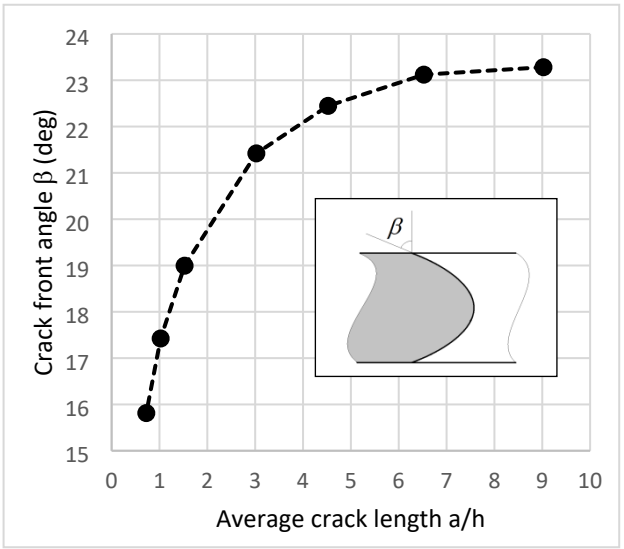

Figure 11 – Emerging crack angle vs average crack length.

In figs. 10 and 11, the trend of two of the most significative crack front shape parameters are reported at increasing opening displacement: the vertex curvature B/R_C, and the intersection angle β

between the crack front and the external surfaces. Both parameters increase with the increasing of average crack length *a/h*. This is probably due to the combination of the following occurrences: the shorter cracks are influenced by the detail of the boundary conditions more than the longer ones; further, the average crack length influences the ratio between the bending moment and the shear near to the crack front.

Many authors, mentioning among the others Pook (1994), Heyder and Kuhn (2006), Ševčík et al. (2012), by analysing the stress singularity trend along the crack front, supported the existence of a characteristic intersection angle between the crack front and the external surfaces, only depending on the Poisson's ratio of the material. The results reported in fig. 11 do not support this hypothesis. Even within the same DCB model, the intersection angle results different at different crack lengths: in fact, it varies within the range $\beta \approx 16° \div \beta \approx 23°$ when the average crack varies in the range $a/h \approx 1 \div a/h \approx 10$.

Actually, Zakavi et al. (2021) have highlighted that this problem has not yet a common solution; in fact, one can find in literature a very wide range of experimental outcomes for the intersection angle (the authors have reported $\beta \approx 10° \div 40°$). A database of rigorous numerical results for this angle for different geometries, crack configurations and boundary conditions could be provided by a systematic application of the present methodology.

5 – Crack front shape verification by comparison with a cohesive elements model

Within the variational framework, the hypothetical convergence of cohesive type models to Griffith-like models can be easily framed in the language of Γ-convergence (Francfort et al., 2008). Taking advance of this property, in this section we have realized a comparison between the crack front shape calculated in the previous section 4 and the one obtained by modelling the crack surface with interface cohesive elements (cohesive zone model, CZM).

As well known, such a model cannot exactly define a crack front where a stress singularity arises; instead, it defines a process zone, with a finite area, without singularities. The main parameters of a CZM are the fracture energy and the process zone characteristic length. At any fixed value of the fracture energy J_C, the smaller the process zone length, the higher the maximum cohesive stress. When the process zone length approaches to zero, the stress field tends to reproduce the singularity present in the sharp crack model. For the present verification, the following exponential cohesive model, due to Xu and Needleman (1994) was utilized:

$$\sigma_{co}(x,y) = J_c \frac{v(x,y)}{v_r^2} \exp\left(-\frac{v(x,y)}{v_r}\right) \tag{71}$$

In equation (71), σ_{co} is the normal cohesive stress, v is the relative displacement between the two crack surfaces, and v_r a scale parameter, related to the characteristic length of the process zone, which is inversely proportional to the maximum σ_{co} value. Once the crack propagation calculation has run, at each load step a map $v(x,y)$ of the surfaces' relative displacements is provided as output. As already said, the crack front line isn't uniquely defined; therefore, the equivalent pointwise crack length was defined here as the length corresponding to the same total damage level χ calculated with the CZM, that is:

$$a(y) = a_{in} + \int_{a_{in}}^{L} \chi(v(x,y))dx; \quad \chi(v(x,y)) = 1 - \exp\left(-\frac{v(x,y)}{v_r}\right) \tag{72}$$

To the aim approaching the sharp crack solutions, the scale parameter v_r must be as small as possible. Unfortunately, the lower v_r, the higher the cohesive elements minimum number, and more difficulty the convergence. The minimum value of the scale parameter we were able to reach, before running into convergence problems, was v_r/B = 0.0001. The interface mesh was made with square cohesive elements, having the side length *B/100*. Actually, this mesh is more detailed and regular than the one utilized in section 4 for the surface integrals calculations. For comparison, our FE model with the sharp crack has about 100000 nodes, whereas our FE model with the CZM has about 400000 nodes.

In fig. 12 is qualitatively depicted the interface normal stress σ_y resulting from the two calculation methodologies under consideration; of course, due to the singularity, at the crack front nodal points the sharp crack stress field cannot be convergent. However, even this qualitative comparison highlights that at the same load the crack lengths and shapes are very similar.

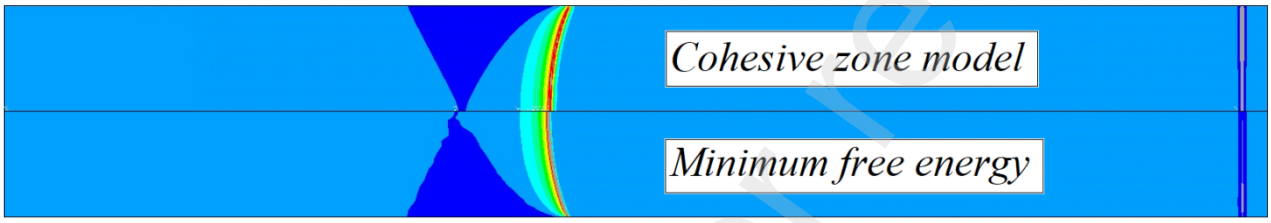

Figure 12 – Qualitative comparison of the interface normal stress resulting from the cohesive zone model and minimum free energy methodology

In figs. 13 and 14 a quantitative comparison of the crack front shape is reported. In particular, the two pictures report two comparisons, for a small and a long crack, represented at the same lengths scaling, whose shapes result to be significantly different. The comparison shows that the new results presented in the section 4 of this work are very close to the ones obtainable using a very detailed cohesive interface model, even in the neighbourhood of the external surfaces. Since the two results have been obtained using two completely different methodologies, this comparison corroborates the correctness of the numerical outcomes presented in section 4 and the underlying theory.

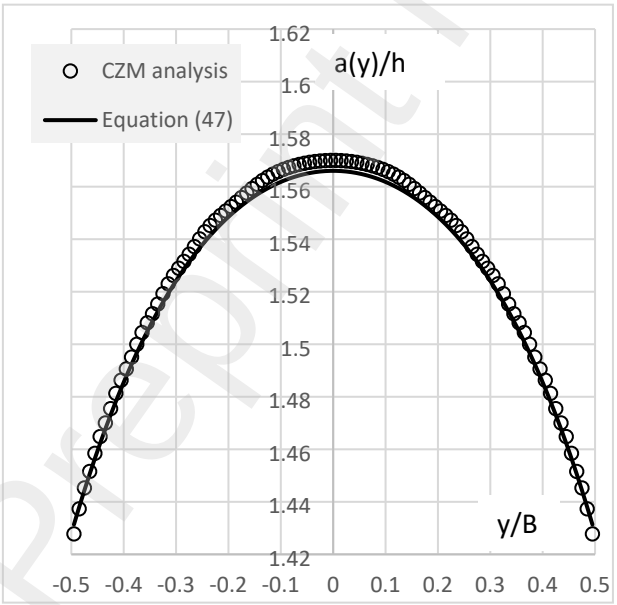

Figure 13. Crack front shape at δ/h=0.023

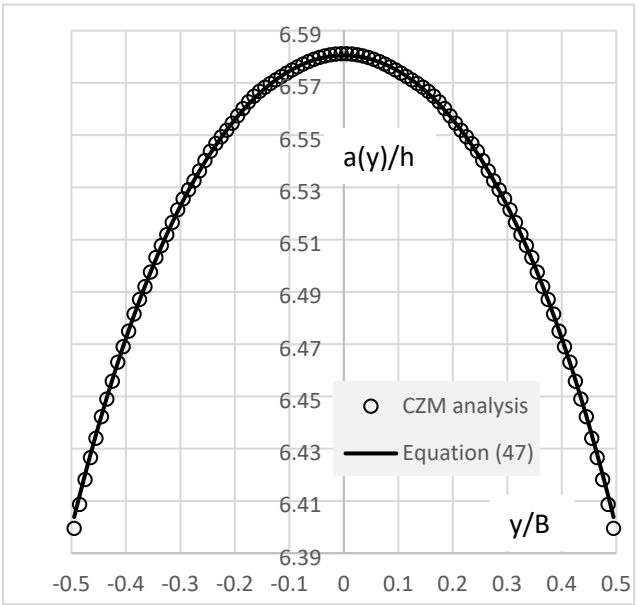

Figure 14. Crack front shape at δ/h=0.241

6 - Conclusions

In this work, the crack front quasi-static evolution in a three-dimensional brittle domain was faced, using only the elastic properties, the fracture energy, and a stationarity principle. In the first part, we showed that, introducing the variable 'crack front shape' and the fracture energy in the total free energy computation, the equilibrium of an elastic domain with a brittle crack can be mathematically considered as a constrained stationarity problem. In particular, the solution of this problem provides the exact crack front shape at equilibrium with a given load. It states that, at each point of the crack front, the (unitary) fracture potential – which is a quantity generalising the pointwise energy release rate – is not higher than the (unitary) fracture energy. Eventually, this condition has a form very similar to the pointwise Griffith criterion, but its interpretation is subtly different from the one most adopted in literature. In fact, as usually interpreted, the Griffith criterion establishes a propagation condition (i.e., 'the crack propagates if…'); instead, the way we attained the result suggest a static condition (i.e., 'the crack is at equilibrium if…'). In our opinion, this interpretation also deserves to be closely considered.

Next, we calculated the fracture potential taking advantage of the De Lorenzi's formulation of the energy released due to a general virtual crack increment. As a result, we found that, at each point of the crack front, the fracture potential can be calculated by summing some line and surface integrals. The individual values of these integrals depend on the single integration domain shape, area, and orientation, but their sum depends only on the position of the integration domain along the crack front. If the integration domains were chosen orthogonal to the crack front, we would obtain as degenerated cases various domain integrals well known in literature. On the other hand, exploiting the opportunity to use integration domains non orthogonal to the crack front, one can use a very regular FE mesh, and obtain, in turn, very accurate evaluations of the fracture potentials. Further, contrarily to the traditional techniques, they can be rigorously calculated even in the neighbourhood of the external surfaces.

Then, we presented a calculation technique for the quasi-static crack evolution, consisting of stepping from an equilibrium condition to the next one using only the general equilibrium conditions previously pointed out. Hence, no propagation criterion needs to be introduced, like the maximum dissipation power or the maximum energy release rate, since the crack front shape at equilibrium is totally determined by the static conditions. In particular, with this methodology, one doesn't need introducing a propagation constitutive law. However, in this context, any external propagation criteria provided by the literature can be used as predictor of the unknown crack front in the iterative calculation algorithm.

As a benchmark, we applied this scheme for calculating the crack front shape of a DCB specimen FE model, and the results we obtained are fully compliant with the experimental outcomes reported in literature. Finally, we verified these results by comparing them with the outcomes of a completely different methodology, that is the cohesive interface model. The crack front shapes resulting by the two methodologies matches each other very soundly.

The methodology presented in this work provides a rigorous framework for calculating the evolution of the plane brittle cracks in elastic three-dimensional domains. It can also be used with interfacial fractures between different materials, nonlinear elastic materials and anisotropic materials. In principle, once added opportune modifications, this methodology could be also used for calculating the evolution of generally non-plane brittle cracks.

References

Amestoy, M., Bui, H.D., Labbens, R., On the definition of local path independent integrals in 3D crack problems, Mech. Res. Communications (1981).

Blackburn W.S., Path independent integrals to predict onset of crack instability in an elastic plastic material, International Journal of Fracture Mechanics, 8 (1972), pp. 343-346.

Casal, P., Interpretation of the Rice integral in continuum mechanics, Lett. Appl. Engng. Sci. (Int. J. Engng. Sci.) 16 (1978), 335–347.

De Lorenzi H.G., On the energy release rate and the J-integral for 3-D crack configurations, Int. Journ. of Fracture 19 (1982) 183-193.

Destuynder Ph., Djaoua M., Sur une interprétation mathématique de l'intégrale de Rice en théorie de la rupture fragile, Math. Meth. in the Appl. Sci. 3 (1981) 70-87.

Eriksson K., A domain independent integral expression for the crack extension force of a curved crack in three dimensions (2002), Journal of the Mechanics and Physics of Solids, 50 (2), pp. 381 – 403.

Eshelby J.D., The elastic energy-momentum tensor (1975), Journal of Elasticity, Vol. 5, Nos. 3-4.

Francfort G.A., Bourdin B., Marigo J.-J., The variational approach to fracture (2008), Journal of Elasticity, 91 (1-3), pp. 5 – 148.

Galdos R., A finite element technique to simulate the stable shape evolution of planar cracks with an application to a semi-elliptical surface crack in a bimaterial finite solid (1997), International Journal for Numerical Methods in Engineering, 40 (5), pp. 905 - 917.

Giner E., Fernández-Zúñiga D., Fernández-Sáez J., Fernández-Canteli A., On the Jx1-integral and the out-of-plane constraint in a 3D elastic cracked plate loaded in tension, International Journal of Solids and Structures, Volume 47, Issues 7–8, 2010, pp. 934-946.

Griffith, A. A.; The phenomena of rupture and flow in solids (1921), Philosophical Transactions of the Royal Society of London, A, 221 (582–593): 163–198.

Gürses E., Miehe C., A computational framework of three-dimensional configurational-force-driven brittle crack propagation, Computer Methods in Applied Mechanics and Engineering, 198, Issues 15–16, 2009, pp. 1413-1428.

Gurtin M.E., Podio-Guidugli P., Configurational forces and the basic laws for crack propagation (1996), Journal of the Mechanics and Physics of Solids, 44 (6), pp. 905 - 927.

Heyder M., Kuhn G. 3D fatigue crack propagation: experimental studies. Int J. Fatigue 2006; 28:627–34.

Jiang Z., Wan S., Keller T., Fang Z., Vassilopoulos A.P., Influence of curved delamination front on R-curve of DCB specimen (2019), Composite Structures, 227, art. no. 111311.

Kaczmarczyk, Ł., Nezhad, M.M. and Pearce, C. (2014), Three-dimensional brittle fracture: configurational-force-driven crack propagation. Int. J. Numer. Meth. Engng, 97: 531-550.

Kaczmarczyk, L., Ullah, Z., Pearce, C. J.; Energy consistent framework for continuously evolving 3D crack propagation (2017). Comput. Methods Appl. Mech. Engrg. 324 (2017) 54–73.

Kuhn C., Müller R., A continuum phase field model for fracture (2010) Engineering Fracture Mechanics, 77 (18), pp. 3625 - 3634.

Kuhn, H. W.; Tucker, A. W. (1951). "Nonlinear programming". Proceedings of 2nd Berkeley Symposium. Berkeley: University of California Press. pp. 481–492.

Li F.Z., Shih C.F., Needleman A., A comparison of methods for calculating energy release rates, Engineering Fracture Mechanics, Volume 21, Issue 2 (1985) pp. 405-421.

Maugin G.A., Sixty years of configurational mechanics (1950–2010), Mechanics Research Communications, Volume 50 (2013), pp. 39-49.

Maugis D., Contact, Adhesion and Rupture of Elastic Solids, Springer series in solid-state sciences, ISSN 0171-1873; 130, Springer, New York (2000).

Miehe C., Welschinger F., Hofacker M., Thermodynamically consistent phase-field models of fracture: Variational principles and multi-field FE implementations (2010), International Journal for Numerical Methods in Engineering, 83 (10), pp. 1273 - 1311.

Moran B., Shih C.F., Crack tip and associated domain integrals from momentum and energy balance, Engineering Fracture Mechanics, Volume 27, Issue 6, 1987, pp. 615-642.

Oplt T.,Hutar P., Pokorný P., Náhlík L., Chlup Z., Berto F., Effect of the free surface on the fatigue crack front curvature at high stress asymmetry, International Journal of Fatigue, Volume 118, 2019, pp. 249-261.

Pook, L.P. Some implications of corner point singularities. Eng. Fract. Mech., 48 (1994), pp. 367–378.

Riks E., An incremental approach to the solution of snapping and buckling programs, Solids & Structures, Vol. 15, pp. 529-51, 1979.

Ševčík M., Hutař P., Zouhar M., Náhlík L., Numerical estimation of the fatigue crack front shape for a specimen with finite thickness, International Journal of Fatigue, Volume 39 (2012), pp. 75-80.

Steinmann P., Ackermann D., Barth F.J., Application of material forces to hyperelastostatic fracture mechanics. II. Computational setting (2001), International Journal of Solids and Structures, 38 (32-33), pp. 5509 – 5526.

Suo X.Z., Combescure A., On the application of G(Θ) method and its comparison with De Lorenzi's approach, Nuclear Engineering and Design, Volume 135, Issue 2, 1992, pp. 207-224.

Vu M.N., Geniaut S., Massin P., Marigo J.J., Numerical investigation on corner singularities in cracked plates using the G-theta method with an adapted θ field, Theoretical and Applied Fracture Mechanics, 77 (2015), pp. 59-68.

Xu X.P., Needleman A., Numerical simulations of fast crack growth in brittle solids, Journal of the Mechanics and Physics of Solids. Vol. 42 (1994), pp. 1397-1434.

Zakavi B., Kotousov A., Branco R., Does the front of fatigue crack intersect free surface at critical angle?, Theoretical and Applied Fracture Mechanics, 114 (2021), 102985.